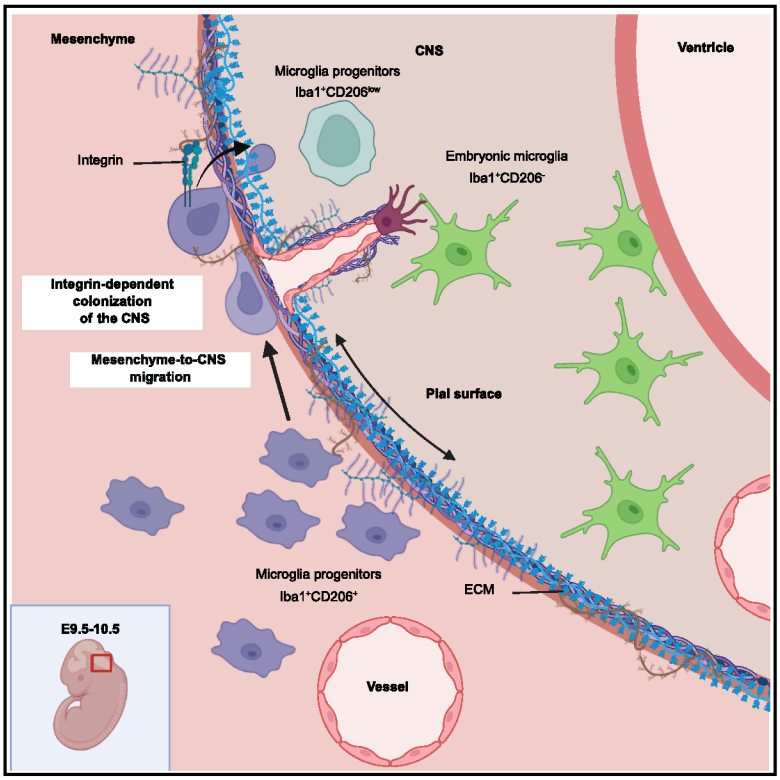
Article

Developmental Cell

Early microglia progenitors colonize the embryonic CNS via integrin-mediated migration from the pial surface

Graphical abstract



Authors

Philippe Petry, Alexander Oschwald, Simon Merkt, ..., Marco Prinz, Tim Lämmermann, Katrin Kierdorf

Correspondence

katrin.kierdorf@uniklinik-freiburg.de

In brief

Petry et al. demonstrate a defined migration route of microglia progenitors from the surrounding mesenchyme into the embryonic CNS. This process relies on integrin activation and interactions with the ECM-rich pial surface, highlighting a previously unrecognized migration route and molecular requirements for early microglia colonization of the CNS.

Highlights

- Microglia progenitors enter the embryonic CNS from the surrounding mesenchyme
- ECM-integrin interactions facilitate microglial progenitor migration into the CNS
- Early microglial colonization of the CNS is talin-1 dependent

Petry et al., 2026, Developmental Cell *61*, 85–101
January 14, 2026 © 2025 The Author(s). Published by Elsevier Inc.
https://doi.org/10.1016/j.devcel.2025.08.012

CellPress

Developmental Cell

CellPress
OPEN ACCESS

Article

Early microglia progenitors colonize the embryonic CNS via integrin-mediated migration from the pial surface

Philippe Petry,[1,2,13] Alexander Oschwald,[1,2,13] Simon Merkt,[3,4,5] Thien-Ly Julia Dinh,[2,6] Geoffroy Andrieux,[7] Cylia Crisand,[1] Hannah Botterer,[1] Elisa Nent,[8] Neil Paterson,[8] Monique Havermans,[1,2] Roman Sankowski,[1] Oliver Schilling,[6] Melanie Boerries,[7,9] Lukas Amann,[1] Olaf Groß,[1,10] Andreas Schlitzer,[3] Marco Prinz,[1,10] Tim Lämmermann,[8,11] and Katrin Kierdorf[1,10,12,14,*]

[1]Institute of Neuropathology, Faculty of Medicine, Medical Center-University of Freiburg, 79106 Freiburg, Germany
[2]Faculty of Biology, University of Freiburg, 79104 Freiburg, Germany
[3]Biology of Inflammation, Life and Medical Sciences (LIMES), University of Bonn, 53115 Bonn, Germany
[4]Department of Systems Immunology and Proteomics, Institute of Innate Immunity, Medical Faculty, University of Bonn, 53127 Bonn, Germany
[5]Bonn Center for Mathematical Life Sciences, University of Bonn, 53115 Bonn, Germany
[6]Institute of Pathology, Faculty of Medicine, Medical Center-University of Freiburg, 79106 Freiburg, Germany
[7]Institute of Medical Bioinformatics and Systems Medicine (IBSM), Medical Center-University of Freiburg, Faculty of Medicine, University of Freiburg, 79110 Freiburg, Germany
[8]Max Planck Institute of Immunobiology and Epigenetics, 79108 Freiburg, Germany
[9]German Cancer Consortium (DKTK), Partner site Freiburg, a partnership between DKFZ and Medical Center-University of Freiburg, 79106 Freiburg, Germany
[10]Signalling Research Centres BIOSS and CIBSS, University of Freiburg, 79104 Freiburg, Germany
[11]Institute of Medical Biochemistry, Center for Molecular Biology of Inflammation (ZMBE), University of Münster, 48149 Münster, Germany
[12]Institute for Infection Prevention and Control, Faculty of Medicine, Medical Center-University of Freiburg, 79106 Freiburg, Germany
[13]These authors contributed equally
[14]Lead contact
*Correspondence: katrin.kierdorf@uniklinik-freiburg.de
https://doi.org/10.1016/j.devcel.2025.08.012

SUMMARY

Macrophage progenitors colonize their anatomical niches in the central nervous system (CNS) in distinct pre- and postnatal waves. Microglia progenitors originate from early erythromyeloid progenitors in the yolk sac and enter the murine CNS around embryonic day (E)9.5. While their developmental origin is well established, the molecular mechanisms guiding CNS colonization are not yet resolved. Using transcriptomic and proteomic approaches, we identified potential factors involved in this process. Microglia progenitors showed a distinct integrin surface profile and transmigrate along the extracellular matrix (ECM)-enriched pial surface into the CNS, pointing to a mesenchyme-to-CNS migration route. Loss of the integrin adaptor protein talin-1 in microglia progenitors led to a reduced CNS colonization, whereas macrophage progenitors in the surrounding mesenchyme remained unchanged. Overall, our data suggest that microglial progenitors enter the CNS parenchyma via talin-1-mediated migration from the surrounding mesenchyme through the ECM-enriched pial surface.

INTRODUCTION

The central nervous system (CNS) is colonized by macrophage progenitors in coordinated waves during pre- and postnatal development.[1–3] Distinct long-lived macrophage populations in the CNS parenchyma and interfaces originate from fetal progenitors, including microglia, perivascular, intraventricular, and leptomeningeal macrophages, while stromal choroid plexus and subsets of dural macrophages arise from adult hematopoietic stem cells.[4–7] In mice, the CNS is initially colonized by microglia progenitors around embryonic day (E)9.5[8–10] followed by microglia expansion until their mature adult network is established.[11–13] Microglia progenitors arise from early erythromyeloid progenitors (EMPs) in the extraembryonic yolk sac (YS) and colonize the embryo subsequently.[14,15] Different EMP-derived myeloid/macrophage progenitors were defined in the embryonic YS[10,16], including a $CD45^+ckit^+CX_3CR1^-CD11b^{-/+}F4/80^-$ intermediate myeloid progenitor (A1 progenitor) differentiating to a $CD45^+ckit^-CX_3CR1^+CD11b^+F4/80^+$ macrophage progenitor (A2 progenitor or pre-macrophage).[10,17,18] Recently, we and others showed that within the A2 progenitor population, two subsets exist, including a *mannose receptor C-type 1* (*Mrc1*;

This is an open access article under the CC BY license (http://creativecommons.org/licenses/by/4.0/).

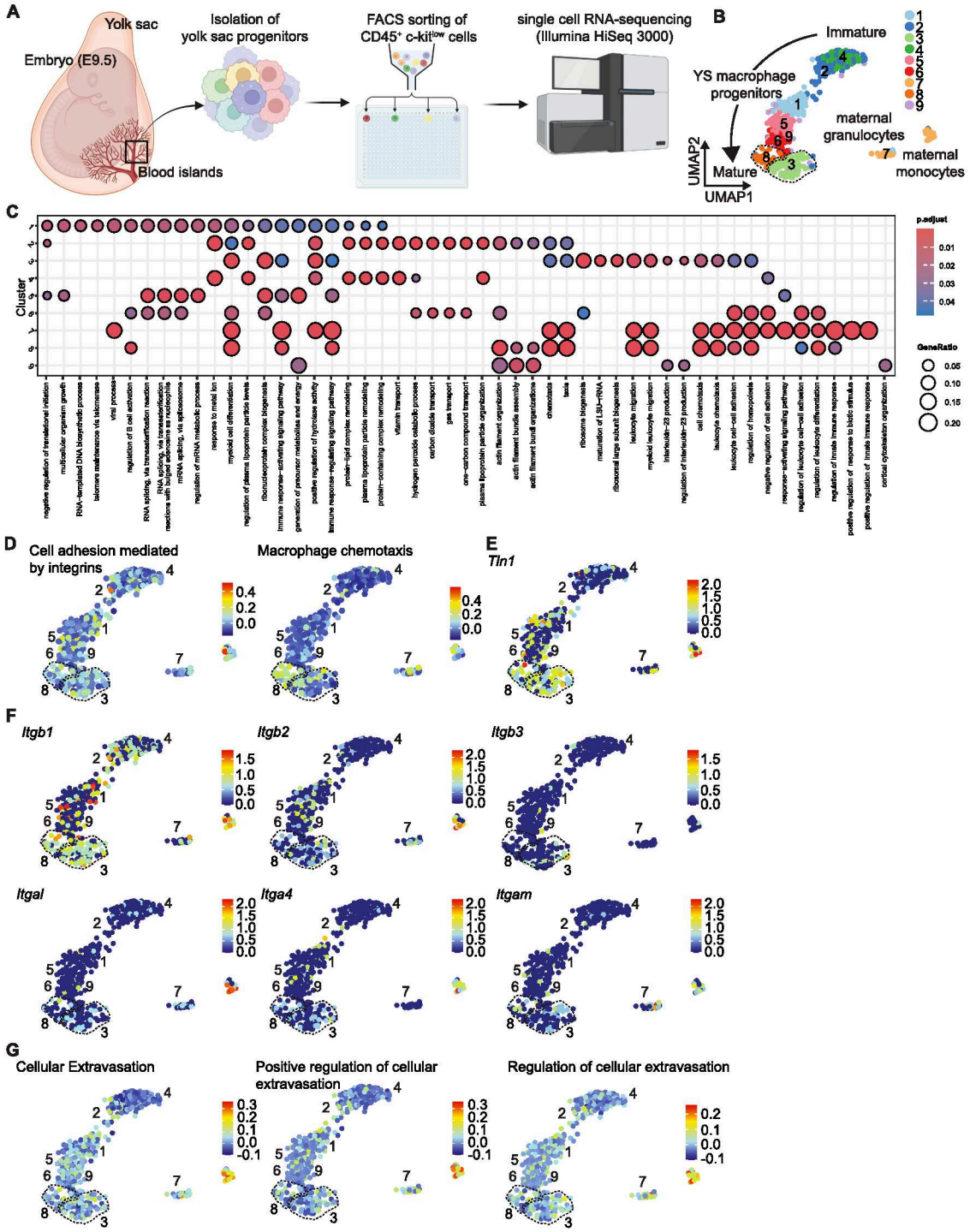


Figure 1. Macrophage progenitors in the yolk sac, especially *Mrc1*$^{+}$ progenitors, express high levels of genes associated with cell migration and cell adhesion

(A) Workflow of scRNA-seq analysis of CD45^{+} c-kit^{low} YS progenitors at E9.5. Created in BioRender: Kierdorf, K. (2025) https://BioRender.com/0bmu097.

(B) Uniform Manifold Approximation and Projection (UMAP) plot of cell clusters (C1–C9) identified by unsupervised clustering of analyzed YS progenitors. Each color represents one cell cluster. Cell clusters C3 and C8, representing macrophage progenitors, are outlined by dotted lines. Each dot represents one cell (N = 483).

(C) Gene Ontology (GO) enrichment analysis across cell clusters C1–C9. GO enrichment was based on the top 100 differentially expressed (DE) genes per cell cluster. Dot sizes indicate the ratio of DE genes per cluster over all genes within a given GO term. Color scale in the legend encodes the Benjamini-Hochberg adjusted p value from a one-sided Fisher's exact test.

(legend continued on next page)

CellPress
OPEN ACCESS

encoding: CD206)$^+$ progenitor, which gives rise to microglia and CNS-associated macrophages (CAMs).[19,20] Besides the "early" colonization wave at E9.5, a second "later" wave of *Mrc1*$^+$ macrophage progenitors was reported to enter the CNS from the mesenchyme via the roof plate between E12.5 and E14.5 and traffic to the CNS pallium through the ventricular system.[21] However, the contribution of this wave to the overall adult microglia population remains to be defined.

So far, only a few studies have focused on the precise mechanisms guiding early microglia colonization of the embryonic CNS. It was suggested that EMPs and macrophage progenitors migrate to the embryo via the developing blood circulation, and microglia progenitors extravasate from blood vessels into the CNS.[9,22] Previously, we revealed a role of matrix metalloproteinases-8 (MMP-8) and -9 (MMP-9) for the migration of microglia progenitors into the embryonic CNS.[10] In zebrafish, microglia progenitor recruitment was demonstrated to rely on interleukin-34 (IL-34)/colony-stimulating factor 1 receptor (CSF1R) signaling.[23] Additionally, neuronal apoptosis in the optical tectum of zebrafish larvae was described as a key signal for microglia progenitor recruitment mediated by nucleotide signaling,[24] as well as lysophosphatidylcholine/gp132b signaling.[25]

To gain insights into the initial microglial CNS colonization, we combined transcriptomic and proteomic approaches to elucidate key factors involved. Our study reveals that early CNS colonization by microglia progenitors occurs along the extracellular matrix (ECM)-enriched pial surface where cells migrate into the CNS parenchyma, and this migration is integrin dependent.

RESULTS

Microglia progenitors exhibit an enriched expression of genes associated with chemotaxis, cell adhesion, and ECM remodeling

To identify factors involved in the recruitment of microglia progenitors from the YS into the developing CNS, we took advantage of our previously generated single cell RNA-sequencing (scRNA-seq) dataset of myeloid YS progenitors[20] (Figure 1A). As characterized before,[20] microglia progenitors were mainly located in the clusters (C)3 and C8 (Figure 1B), distinguished by low *Mrc1* expression (*Mrc1*$^-$) in C3 and higher expression levels within C8 (*Mrc1*$^+$).[20] First, we defined the cluster-wise enriched top Gene Ontology (GO) terms. C3 and C8 showed a higher abundance of genes associated with GO terms of cell differentiation, including "myeloid cell differentiation," but also GO terms such as "leukocyte migration" and "myeloid leukocyte migration" (Figure 1C). Especially, C8 showed an enrichment for genes within GO terms associated with cell migration, such as "chemotaxis" or "leukocyte cell-cell adhesion" (Figure 1C). Additionally, higher abundance of GO terms such as "cell adhesion mediated by integrins" and "macrophage chemotaxis" was detected (Figure 1D). Genes involved in integrin-mediated adhesion were enriched in both Cs, including integrin adaptor protein *talin-1* (*Tln-1*) (Figure 1E), integrin β subunits *Itgb1*, *Itgb2*, and *Itgb3*, and integrin α subunits *Itgal*, *Itga4*, and *Itgam* (Figure 1F). Integrins are heterodimeric adhesion molecules formed by one α and one β subunit. A single β subunit can pair with multiple different α subunits.[27] They assist cell migration and adhesion to other cells or ECM. Especially their role during leukocyte extravasation from the vasculature during inflammation is well described. Interestingly, we could not find an enrichment of GO terms associated with classical extravasation of leukocytes from blood vessels into inflamed tissues in microglia progenitors (Figure 1G). Our analysis revealed a profound induction of genes associated with leukocyte migration and chemotaxis in microglia progenitors from the YS, but not genes associated with classical extravasation of leukocytes from vasculature.

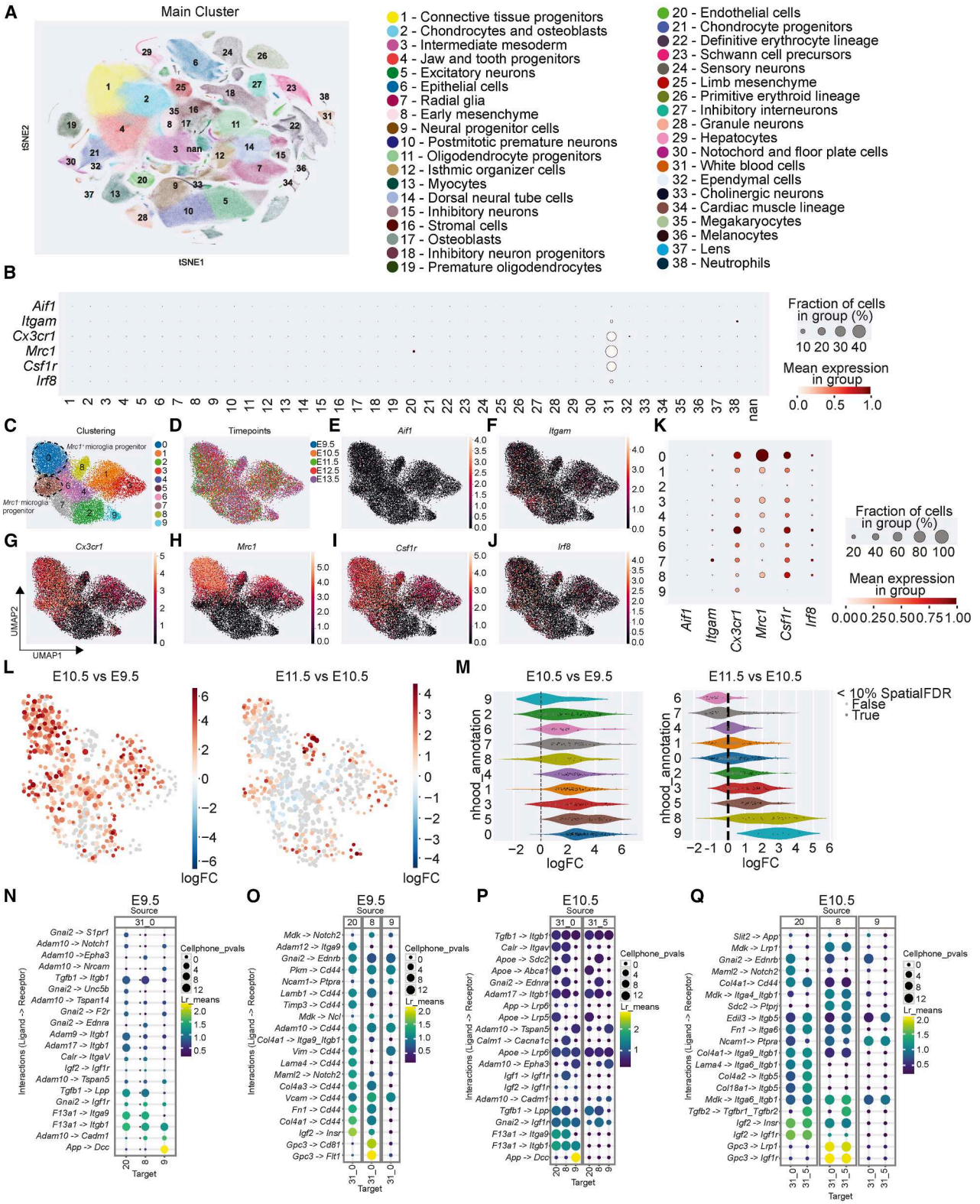
To gain insights into the profile of microglia progenitors and their potential molecular interactions during CNS colonization, we took advantage of a published scRNA-seq dataset of the developing mouse embryo.[28] Following t-distributed stochastic neighbor embedding (t-SNE) for dimension reduction, clusters were annotated according to the established cell state signatures of the original publication[28] (Figure 2A). We investigated the distribution of microglia progenitors across all annotated cell clusters using *Aif1*, *Itgam*, *Cx3cr1*, *Mrc1*, *Csf1r*, and *Irf8* as key signature genes, as described before.[18–20] Cells with a microglia progenitor signature were enriched in C31, annotated as white blood cells (Figure 2B). Since C31 contained signatures of different blood cells, we performed sub-clustering of C31 to determine the distribution of cells with a microglia progenitor signature across the different sub-clusterss (Table S1; Figure 2C). We identified ten sub-clusters (C31_0–C31_9) across the different developmental stages (E9.5–13.5) (Figures 2D and S1A–S1F). Differentially expressed (DE) genes of the sub-clusters were used to annotate microglia progenitor signatures (Figures 2E–2K and S1G; Table S1). Sub-clusters C31_0 and C31_5 showed a clear enrichment for the microglia progenitor signature (Figures 2E–2K and S1G; Table S1). In line with previous studies, the sub-cluster C31_5 did not express *Mrc1* (Figures 2E–2K).[19,20] Hence, the two sub-clusters, C31_0 and C31_5, represent the two previously described states of microglia progenitors in the mouse embryo (*Mrc1*$^-$ and *Mrc1*$^+$ progenitors). At E9.5, the sub-cluster of *Mrc1*$^+$ progenitors (C31_0) was highly abundant, whereas *Mrc1*$^-$ progenitors (C31_5) were barely found (Figures S1A–S1F). Differential abundance was tested using Milo,[29] and both progenitor sub-Cs, C31_0 and C31_5, were enriched at E10.5 vs. E9.5, whereas other sub-Cs

(D) UMAP feature plots depicting the enrichment of genes associated with the GO terms "cell adhesion mediated by integrins" (GO:0033627) (left) and "macrophage chemotaxis" (GO:0048246) (right). Color scale indicates the average expression of the specified gene program, and minus indicates the average expression of randomly selected background genes.[26]

(E) UMAP feature plots depicting the expression of *Tln1*.

(F) UMAP feature plots depicting the expression of *Itgb1*, *Itgb2*, *Itgb3*, *Itgal*, *Itga4*, and *Itgam*. Color scale corresponds to Pearson's residuals from a regularized negative-binomial regression.

(G) UMAP feature plots depicting the enrichment of genes associated with the GO terms "cellular extravasation" (GO:0045123) (left), "positive regulation of cellular extravasation" (GO:0002693) (middle), and "regulation of cellular extravasation" (GO:0002691) (right). Color scale indicates the average expression of the specified gene program, and minus indicates the average expression of randomly selected background genes.[26]



8: Early mesenchyme, 9: Neural progenitor cells, 20: Endothelial cells, 31_0: *Mrc1*$^{+}$ microglia progenitors, 31_5: *Mrc1*$^{-}$ microglia progenitors

(legend on next page)

of C31 were less abundant (Figures 2L and 2M). This enrichment substantially decreased when we compared E11.5 vs. E10.5 (Figures 2L and 2M), showing a clear peak of microglia progenitor signature during early CNS colonization (Figures 2L and 2M). Next, we characterized cellular interactions and signaling pathways of microglia progenitors during CNS colonization. Cell-cell communication analysis using CellPhoneDB[30] did not reveal a preferential interaction with a defined cell cluster at E9.5 and E10.5 (Figure S1H; Tables S2 and S3). Therefore, we tested the interaction between both microglia progenitor sub-clusters and C20 (endothelial cells), C8 (early mesenchyme), and C9 (neural progenitor cells) at E9.5 and E10.5. We identified predicted interactions at E9.5 between *Mrc1*$^{+}$ progenitors (C31_0) and structural clusters C20, C8, and C9, and at E10.5 between those and both progenitor sub-clusters (C31_0 and C31_5) (Figures 2N–2Q). These comprised signaling pathways involved in cell migration, cell-cell adhesion, or breakdown of ECM within the top 20 predicted interactions. For example, ECM genes, e.g., *Fn1*, *Lama4*, and *Col4a1*, expressed by C20 and C8, were suggested to interact with integrins, e.g., *Itga9*/*Itgb1* and *Itga6*/*Itgb1*, and other cell adhesion molecules, e.g., *Cd44*, on microglia progenitors at both time points. Of note, we also found at E10.5 different growth factors and their receptors within the top 20 predicted interactions, including *Tgfb2* expressed by C20 and C8 and the receptor subunits *Tgfbr1* and *Tgfbr2* on the *Mrc1*$^{-}$ microglia progenitor sub-cluster (C31_5). Moreover, we found *Igf2* expressed by C20 and C8, and *Igf1r* expressed by both microglia progenitor sub-clusters. Overall, our analysis suggests an interaction of integrins with ECM during the migration of microglia progenitors to the developing CNS.

Microglia and their progenitors express a heterogeneous and highly dynamic integrin profile across development

Next, we performed extensive profiling of integrin surface expression on macrophage progenitors (A1 and A2 progenitors from the YS at E10.5), embryonic microglia (E10.5, E12.5, E14.5, and E17.5), and adult microglia postnatal day (P)60 (Figures 3 and S2). We identified heterogeneous expression patterns of integrin α and β subunits across all time points analyzed. Surface expression of integrins α_2, β_4, β_5, and β_7 was not detected on progenitors or microglia across development (Figure S3). Integrin subunit α_E was expressed on embryonic microglia; however, the respective subunit, β_7, was not detected (Figure S3). Notably, expression of integrin α subunits α_1, α_3, α_7, α_8, α_9, α_{10}, and α_{11}, as well as integrin β subunits β_6 and β_8, was not analyzed due to technical limitations and lack of suitable antibodies. Integrin β_1 and β_2 subunits were constantly expressed, whereas integrin α subunits were dynamically regulated, pointing to a distinct repertoire of integrins on microglia across development. Integrins $\alpha_M\beta_2$ (CD11b/CD18 and Mac-1) (Figure S2), $\alpha_5\beta_1$ (fibronectin receptor), and $\alpha_6\beta_1$ (laminin receptor) were stably expressed on microglia (Figures 3A and 3B). Integrin subunit α_v, building heterodimers with integrin β subunits β_1, β_3, and also β_8, was also stably expressed. By contrast, integrin $\alpha_x\beta_2$ (CD11c/CD18) was only detected on microglia at E17.5 (Figure 3A). Integrins such as $\alpha_4\beta_1$ (very late antigen-4 [VLA-4]), $\alpha_L\beta_2$ (lymphocyte function-associated antigen 1 [LFA-1]), and $\alpha_{IIb}\beta_3$ (platelet GPIIb-IIIa) were specifically expressed on YS progenitors and early embryonic microglia at E10.5 but were absent at later stages (Figures 3A and 3B). Overall, our findings revealed a dynamic regulation of integrins during microglia development, with a distinct integrin expression profile on microglia progenitors during CNS colonization.

Induction of ECM-related proteins is a core signature of the developing CNS at E9.5

To elucidate which potential factors in the developing CNS facilitate the recruitment of microglia progenitors at E9.5, we dissected CNS tissue at E9.5, E14.5, and P60 and performed liquid chromatography-tandem mass spectrometry (LC-MS/MS)-based proteomics (Figure 4A). During the comparison of differential protein abundance, the samples separated well in principal-component analysis (PCA) space according to their

Figure 2. *Mrc1*$^{+}$ progenitors appear before *Mrc1*$^{-}$ progenitors in the mouse embryo at E9.5, with both showing cellular interactions associated with ECM adhesion and remodeling

(A) t-SNE plot visualizing 2,058,562 annotated cells from developing mouse embryos (E9.5, E10.5, E11.5, E12.5, and E13.5). Cells are colored by cluster. Clusters were annotated based on selected marker genes, as in the original publication.[28]

(B) Microglia progenitor gene signature enrichment across all annotated cell clusters. Dot sizes indicate the fraction of cells in percentage within the annotated cell cluster. Color scale in the legend indicates mean expression levels within each group.

(C) UMAP plot of sub-clusters within C31 ("white blood cells") using the Leiden algorithm. Dots represent cells (N = 15,872). Each color represents one cell sub-cluster (C31_0–C31_9). Microglia progenitor sub-clusters clusters C31_0 and C31_5 are outlined by dotted lines.

(D) UMAP plot of cells annotated to developmental time points within C31. Dots represent cells (N = 15,872). Each color represents one developmental time point. Colors are encoded in the legend.

(E–J) UMAP plots depicting the expression of the microglia progenitor signature genes *Aif1* (E), *Itgam* (F), *Cx3cr1* (G), *Mrc1* (H), *Csf1r* (I), and *Irf8* (J). Dots represent cells (N = 15,872). Color scale corresponds to marker abundance in normalized counts.

(K) Microglia progenitor gene signature enrichment across all sub-clusters. Dot sizes indicate cell fraction enriched with gene signature within each sub-cluster. Color scale in the legend indicates mean expression levels within each group normalized per marker.

(L) UMAP plots of cell neighborhoods computed by Milo for abundance testing. Plots show E10.5 vs. E9.5 (left) and E11.5 vs. E10.5 (right). Dot size represents neighborhood size. Color scale represents logarithmic fold change. Non-significant (threshold 0.1) neighborhoods are grayed out.

(M) Violin plots representing differential abundance by Milo mapped to sub-clusters for E10.5 vs. E9.5 (left) and E11.5 vs. E10.5 (right). Color code indicates sub-clusters. Dotted line represents no difference between stages. Individual dots represent individual neighborhoods. Non-significant (threshold 0.1) neighborhoods are grayed out. Logarithmic fold change is plotted.

(N–Q) Dot plots representing the top 20 predicted interaction partners by CellPhoneDB between (N) sub-cluster C31_0 (source) and clusters C20, C8, and C9 (target) at E9.5; (O) clusters C20, C8, and C9 (source) and sub-cluster C31_0 (target) at E9.5; (P) sub-clusters C31_0 and C31_5 (source) and clusters C20, C8, and C9 (target) at E10.5; and (Q) clusters C20, C8, and C9 (source) and sub-clusters C31_0 and C31_5 (target) at E10.5. Dot sizes indicate negative logarithmic p value. Color scale in the legend indicates the mean expression of ligand and receptor.

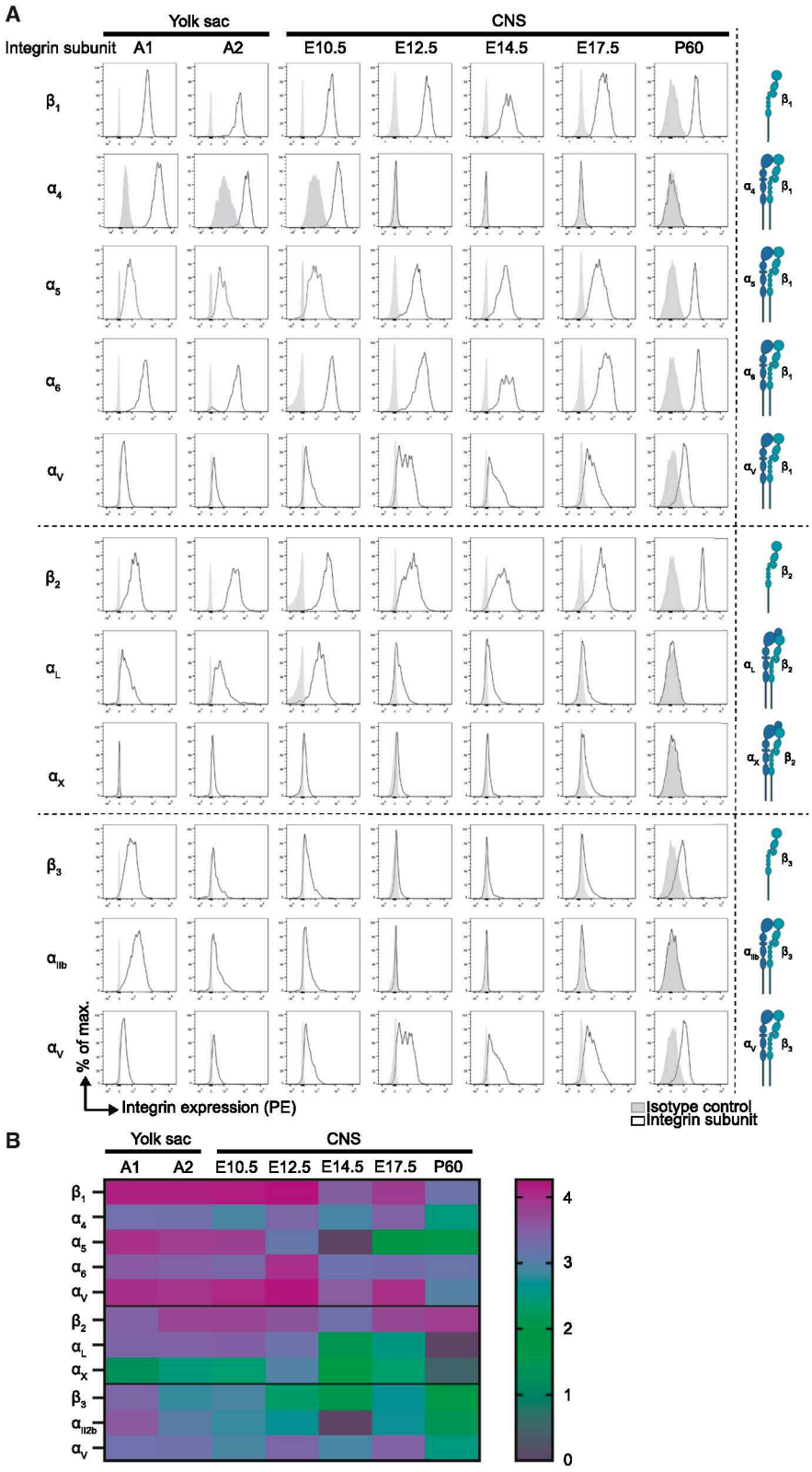


Figure 3. Microglia and yolk sac progenitors equip a dynamic integrin surface profile across development

(A) Flow cytometry analysis of integrin subunits β_1, α_4, α_5, α_6, α_v, β_2, α_L, α_x, β_3, α_{IIb}, and α_v on A1 and A2 progenitors in the YS at E10.5, microglia in the developing CNS at E10.5, E12.5, E14.5, E17.5, and in the cortex at P60. Representative histograms are shown from three to four individual experiments. Isotype control is

(legend continued on next page)

CellPress
OPEN ACCESS

groups (Figure 4B). First, we compared protein abundance in the CNS from E9.5 to P60 and found a high abundance of proteins associated with GO terms of cell proliferation and neuronal differentiation (Figure S4A). Next, we compared protein abundance between E9.5 and E14.5 (Figure 4C). We found a wide range of significantly over-represented proteins associated with GO terms such as "nucleic acid binding," "DNA helicase binding," and "DNA replication" but also "ECM binding," "ECM structural constituent," and "integrin binding" (Figure S4B). ECM proteins, such as laminin subunits, collagen α-1 and α-2 chains, fibronectin, and fibrillin-1, were significantly more abundant in the CNS at E9.5 compared with E14.5 (Figure 4C). Specific GO terms associated with ECM (NABA GO terms)[31,32] confirmed an enrichment with ECM-associated proteins across several NABA GO terms, including "basement membrane" and "ECM glycoproteins" at E9.5 (Figure 4D).

In parallel, we performed bulk RNA sequencing (RNA-seq) from dissected CNS tissue at E9.5, E14.5, and P60 (Figure S5A). Samples separated well in PCA space according to their groups (Figure S5B). Analysis of DE genes (adjusted p value, $p < 0.05$) at E9.5 compared with E14.5 showed a significant induction of genes associated with ECM, such as *Fndc3c1*, *Col9a1*, *Cdh3*, *Lamb1*, *Fbn2*, and *Lama1* (Figure S5C). However, we did not detect an enrichment in specific GO terms associated with ECM or ECM remodeling when we compared E9.5 to E14.5 (Figure S5D) or E9.5 to P60 (Figure S5E). In summary, our data point to a specific increase in ECM and ECM-related proteins in the CNS at E9.5 when the first microglia progenitors colonize the CNS.

Microglia progenitors extensively interact with deposited ECM at the pial surface during colonization of the developing CNS

Based on the results from our transcriptomic and proteomic analyses, we hypothesized that microglia progenitor migration into the CNS could be assisted by integrin-dependent adhesion and migration along deposited ECM. To test this hypothesis, we determined the spatial localization of microglia progenitors during CNS colonization at E9.0 and E9.5. To this end, we took advantage of a recently published spatial transcriptomic dataset of the developing mouse embryo and performed cell annotation according to the original publication.[33] To determine microglia progenitors within the dataset, we used the same microglia progenitor signature (*Aif1*, *Itgam*, *Cx3cr1*, *Mrc1*, *Csf1r*, and *Irf8*) as established above (Figure 2). As expected, we barely detected any microglia progenitors in the embryo at E9.0 (Figures 5A–5C), with only a few cells with this signature associated with the heart, neural tube, and brain (Figure 5C). An increase of cells with a microglia progenitor signature was seen at E9.5, where cells with this signature are enriched in the cell state annotated as "primitive blood progenitors" (Figures 5D–5F). Cells associated with this state were found in close proximity to cells annotated as neural tube and mesenchyme in the head region at E9.5 (Figure 5D). This was reflected by an increase of the microglia progenitor signature in cell states annotated as neural tube and brain, but also mesenchyme (Figure 5F), pointing to an enrichment of cells with a microglia progenitor signature along the border region of the neuroectoderm and the surrounding mesenchyme at E9.5.

Based on this, we hypothesized that microglia progenitors might enter the developing neuroectoderm from the surrounding mesenchyme and tested the spatial distribution of CD206$^+$ and CD206$^-$ microglia progenitors along and within the CNS at E10.5 by immunofluorescence (Figures 6A–6D). Iba-1$^+$CD206$^+$ progenitors form the majority of progenitors in the head mesenchyme, whereas only a few cells were Iba-1$^+$CD206$^-$ (Figure 6E). Along the ECM-enriched pial surface of the CNS, identified by laminin deposition, we found Iba-1$^+$CD206$^+$ progenitors, but no Iba-1$^+$CD206$^-$ cells (Figure 6F). Iba-1$^+$CD206$^+$ progenitors were localized in close proximity and embedded by deposited ECM (Figures 6B–6D). We identified Iba-1$^+$CD206$^+$ progenitors in the process of infiltrating the CNS from the ECM-rich border region, suggesting a potential "mesenchyme-to-CNS" migration (Figures 6B–6D). At E10.5, the first vessels enter the developing hindbrain from the pial surface,[34] and laminin$^+$ vessel-like structures were clearly visible in the hind- and midbrain regions (Figures 6B–6D). However, we could not find Iba-1$^+$CD206$^+$ microglia progenitors in their lumen of developing vessels in the CNS or evidence of a "vessel-to-CNS" extravasation (Figures 6B–6D). Of note, microglia progenitors within the CNS were characterized as Iba-1$^+$CD206$^-$ along with a small number of Iba-1$^+$CD206$^+$ cells, which might account for freshly transitioned progenitors from the pial surface (Figure 6G). This indicates a rapid loss of CD206 as soon as the progenitors enter the CNS parenchyma. Moreover, Iba-1$^+$CD206$^-$ progenitors were in contact with invading blood vessels (Figure 6H), representing potential Tip-macrophages guiding vessel growth as reported before.[35]

Additionally, we analyzed the distribution of Iba-1$^+$CD206$^+$ and Iba-1$^+$CD206$^-$ cells at E12.5 in the CNS (Figures S6A–S6G). We found a peak of Iba-1$^+$CD206$^+$ cells in the ventricle, corresponding to the reported second wave of progenitor infiltration from the roof plate across the ventricle.[21] Similar to E10.5, we did not detect any Iba-1$^+$CD206$^+$ cells in the parenchyma or in association with vessels in the parenchyma (Figures S6D–S6G). At E14.5, we found a clear separation of Iba-1$^+$CD206$^+$ cells in the leptomeninges and Iba-1$^+$CD206$^-$ embryonic microglia in the CNS parenchyma (Figures S6H–S6M), similar to what we have previously reported.[20]

Our data suggest that Iba-1$^+$CD206$^+$ progenitors colonize the developing CNS in an initial wave from the pial surface around E9.5/E10.5, where they migrate along the deposited ECM into the CNS. Upon entrance into the developing neuroectoderm, the progenitors downregulate CD206 and distribute throughout the parenchyma.

Deficiency of *Tln1* results in a reduced migration of microglia progenitors in the developing CNS

Macrophages migrate through interstitial tissue using either amoeboid (integrin-independent) or mesenchymal (integrin-dependent) migration, depending on the tissue context.[36–38] Mesenchymal

depicted alongside each specific integrin subunit antibody. Schematic pairing of integrin α and β subunits is indicated on the right. Created in BioRender: Kierdorf, K. (2025) https://BioRender.com/0bmu097.

(B) Heatmap of mean integrin expression of all analyzed subunits shown in (A). Mean surface expression is shown from three individual experiments normalized to isotype controls. Color code is shown in the legend.

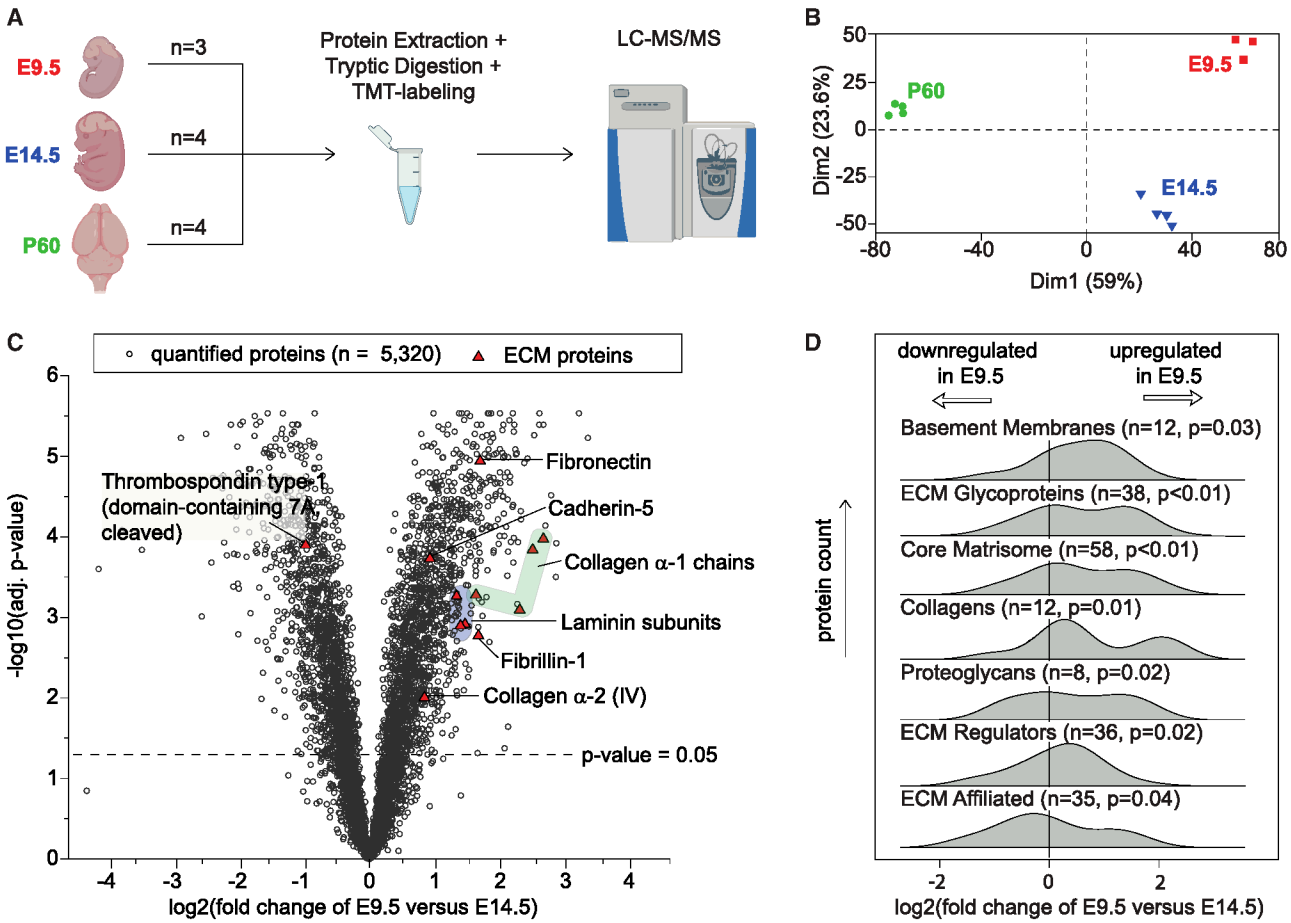


Figure 4. ECM proteins and ECM-associated proteins are enriched in the developing CNS at E9.5

(A) Workflow of LC-MS/MS analysis of the CNS at E9.5, E14.5, and P60. Created in BioRender: Kierdorf, K. (2025) https://BioRender.com/0bmu097.

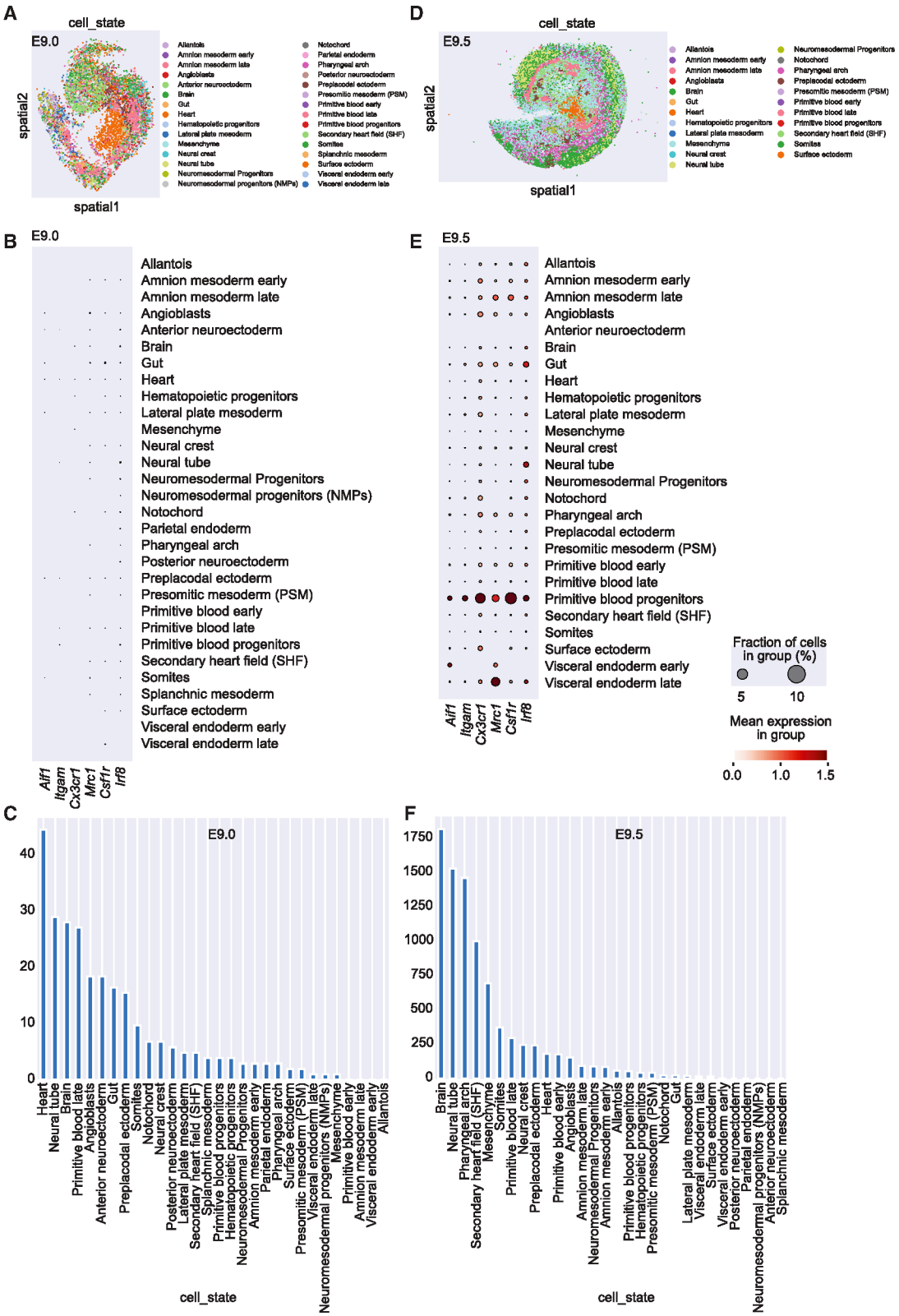
(B) PCA plot depicting distribution of the individual samples. E9.5 (red) $n = 3$, E14.5 (blue) $n = 4$, and P60 (green) $n = 4$.

(C) Volcano plot of DE proteins (adj. p value $p < 0.05$) in the CNS at E9.5 vs. E14.5. 5,320 proteins are shown. Individual ECM proteins of interest are highlighted (red triangles).

(D) Histograms depicting significantly regulated proteins associated with NABA GO terms in E9.5 vs. E14.5. N is the number of detected proteins, and adj. p values are indicated per GO term.

migration requires strong ECM adhesion via high-affinity integrin binding, mediated by the adaptor protein Tln-1.[39,40] We recently showed that perivascular macrophage colonization depends on Tln1-regulated integrin activation.[20] To test if microglia progenitors rely on integrins for the migration from the ECM-enriched pial surface to the CNS, we examined microglia colonization in different integrin-deficient mouse lines at selected developmental time points (Figure 7A). Here, we took advantage of the *Cx3cr1*^{Cre}*Tln1*$^{fl/fl}$ mice to delete *Tln1* in macrophage progenitors from the YS, as we have shown before.[20] First, we analyzed the labeling efficiency of A1 and A2 progenitors in the YS from *Cx3cr1*^{Cre}*Rosa26*$^{LSL\text{-}eYFP}$ mice (Figure S7A) and found an efficient labeling of both progenitor populations (Figure S7B). Next, we compared the number of microglia between *Cx3cr1*^{Cre}*Tln1*$^{fl/fl}$ mice and control littermates in the developing CNS at E10.5. Microglia in the CNS parenchyma were significantly reduced in *Cx3cr1*^{Cre}*Tln1*$^{fl/fl}$ mice compared with control littermates (Figures 7B and 7C). By contrast, we did not find a reduced number of Iba-1^{+} progenitors in the mesenchyme of *Cx3cr1*^{Cre}*Tln1*$^{fl/fl}$ mice (Figures 7B and 7C). These results indicate that migration of microglia progenitors into the CNS depends on *Tln1*, whereas their migration into the mesenchyme was not affected. Next, we tested if *Tln1* deficiency in YS progenitors affects their differentiation toward microglia progenitors. Whereas Tln-1 regulates high-affinity binding of integrins but not their expression per se, we evaluated the surface expression of CD11b (Itgam) and Itgb2 on macrophage progenitors in the YS. Here, we did not detect changes in the expression of CD11b on A1 and A2 progenitors in *Cx3cr1*^{Cre}*Tln1*$^{fl/fl}$ mice compared with controls (Figure S7C). Similarly, Itgb2 was only slightly reduced on A1 progenitors and unaltered on A2 progenitors of *Cx3cr1*^{Cre}*Tln1*$^{fl/fl}$ mice compared with control littermates (Figure S7D). Furthermore, macrophage progenitors in the YS of *Cx3cr1*^{Cre}*Tln1*$^{fl/fl}$ mice showed an unaltered ratio between A2 and A1 progenitors compared with *Tln1*$^{fl/fl}$ mice (Figure S7E). Based on these findings, we propose that the migration of microglia progenitors from the YS to the developing CNS occurs in a two-step process. First, progenitors migrate from the YS to the mesenchyme, a process that is not affected by *Tln1* deficiency

CellPress
OPEN ACCESS



(legend on next page)

and therefore seems to be independent of high-affinity binding by integrins. Second, microglia progenitors colonize the CNS from the surrounding head mesenchyme, a migratory step relying on high-affinity binding of integrins and the interaction with deposited ECM at the pial surface.

Loss of *Itgb2* or *Itgb1* alone does not impair the colonization of the developing CNS by microglia progenitors

Microglia progenitors are equipped with a defined integrin surface pattern during their migration into the CNS, including the particular expression of $\alpha_4\beta_1$ and $\alpha_L\beta_2$ during this migration process (Figure 3). To test the functional role of different integrin subfamilies for this process, we analyzed mice deficient for *Itgb1* in early hematopoietic progenitors ($Vav^{iCre}Itgb1^{fl/fl}$) or *Itgb2*-deficient mice ($Itgb2^{-/-}$). First, we tested the labeling efficiency of the A1 and A2 progenitors in the YS in $Vav^{iCre}Rosa26^{LSL\text{-}eYFP}$ mice (Figure S7F). Our results confirmed an efficient labeling of both progenitor populations with eYFP (Figure S7G). Subsequently, we confirmed a sufficient deletion of Itgb1 surface expression in $Vav^{iCre}Itgb1^{fl/fl}$ on YS progenitors. Itgb1 was efficiently depleted from the surface of A2 progenitors and significantly reduced on A1 progenitors in $Vav^{iCre}Itgb1^{fl/fl}$ compared with $Itgb1^{fl/fl}$ littermates (Figure S7H).

We next tested whether *Itgb1* deficiency affects the differentiation of macrophage progenitors in the YS. We found that $Vav^{iCre}Itgb1^{fl/fl}$ mice have a slight but significant reduction in the ratio of A2 to A1 progenitors compared with $Itgb1^{fl/fl}$ mice (Figure S7I). However, in contrast to $Cx3cr1^{Cre}Tln1^{fl/fl}$ mice, we did not detect a reduction in microglia at E10.5 in the developing CNS of $Vav^{iCre}Itgb1^{fl/fl}$ mice compared with littermate controls (Figures 7D and 7E). Of note, we did not find any differences in macrophage progenitors in the surrounding head mesenchyme of $Vav^{iCre}Itgb1^{fl/fl}$ mice (Figures 7D and 7E). Next, we investigated whether *Itgb1* deficiency affects microglia at later developmental stages. We quantified microglia in the CNS of $Vav^{iCre}Itgb1^{fl/fl}$ mice and littermate controls at E14.5 and P60 but did not detect any differences in cell number between the genotypes (Figures 7D and 7E).

While our results suggest that the migratory transition of microglia from the pial surface into the developing CNS is not dependent on β_1 integrins, we next tested the role of integrin subunit β_2 by taking advantage of *Itgb2*-deficient mice.

We analyzed the surface expression of Itgb2 on A1 and A2 YS progenitors in $Itgb2^{-/-}$ mice compared with the control littermate genotypes, $Itgb2^{+/-}$ and $Itgb2^{+/+}$ (Figure S7J). In $Itgb2^{-/-}$ mice, we found a complete loss of Itgb2 expression on the surface of both progenitor subsets, compared with $Itgb2^{+/+}$ littermate controls (Figure S7J). Of note, $Itgb2^{+/-}$ mice showed a significant reduction in Itgb2 surface expression, but not a complete loss, indicating a haploinsufficient phenotype in these mice (Figure S7J). From the analysis of A1 and A2 progenitor ratios, we could not detect a significant alteration in the YS progenitor compartment between all three genotypes analyzed (Figure S7K). To evaluate the effect of *Itgb2* deficiency on microglia colonization of the CNS, we quantified microglia numbers in the developing CNS at E10.5. Surprisingly, *Itgb2*-deficient mice did not show a reduction in microglia cell number compared with $Itgb2^{+/+}$ mice (Figures 7F and 7G). However, we found a significant increase in the number of microglia in the CNS of haploinsufficient $Itgb2^{+/-}$ mice at E10.5 (Figures 7F and 7G). By contrast, macrophage progenitor number was not affected in the surrounding head mesenchyme in all genotypes (Figures 7F and 7G). At E14.5, the number of microglia equilibrated in $Itgb2^{+/-}$ mice, and all genotypes showed similar cell numbers (Figures 7F and 7G). Accordingly, we did not detect any changes in microglia cell number in adult cortex (Figures 7F and 7G). The loss of either *Itgb1* or *Itgb2* alone did not affect the early colonization of the CNS by microglia progenitors, most likely due to compensatory effects between distinct integrins. Hence, we tested if elevated surface expression of β_2 integrins, such as CD11b (Itgam), on the surface of *Itgb1*-deficient YS progenitors might compensate for this loss. However, we could not find a significant increase in Itgam expression on A1 and A2 progenitors in $Vav^{iCre}Itgb1^{fl/fl}$ mice compared with controls (Figure S7L). Similarly, we could not find a significant increase of Itgb1 on *Itgb2*-deficient YS progenitors, but rather a downregulation in $Itgb2^{-/-}$ and $Itgb2^{+/-}$ mice (Figure S7M). Overall, our results revealed that high-affinity binding of integrins by Tln-1 is an essential contributor to efficient microglia progenitor migration from the pial surface to the developing CNS. Interestingly, our results showed that haploinsufficiency in *Itgb2*, but not *Itgb2* deficiency, can increase the influx of microglia progenitors into the CNS. These findings point to a role of high-affinity integrin binding to guide the adhesion and migratory transition of microglia progenitors from the mesenchyme to the developing CNS.

DISCUSSION

In this study, we provide mechanistic insights on the migration process of microglia progenitors during the initial colonization of the developing CNS.

Several studies, including our own work, reported that microglia progenitors initially colonize the developing murine CNS

Figure 5. Spatial distribution of microglia progenitor signatures is concentrated adjacent to cells of the neuroectoderm and mesenchyme at E9.5

(A) Representative spatial plot of annotated cell states at E9.0 (sample ID = Puck_220718_18 E9.0). Colors and cell annotations are indicated in the legend. Dots represent beads.

(B) Microglia progenitor gene signature enrichment across annotated cell types at E9.0. Dot sizes indicate the fraction of gene-expressing cells in percentage within the annotated cell states across all analyzed sections. Color scale in the legend indicates mean expression levels within each group normalized per gene.

(C) Bar plot indicating the absolute number of detected cells with microglia progenitor signature across annotated cell states at E9.0. Cell states are sorted by microglia progenitor abundance.

(D) Representative spatial plot of annotated cell states at E9.5 (sample ID = 201104_32 E9.5). Colors and cell annotations are indicated in the legend. Dots represent dots.

(E) Microglia progenitor gene signature enrichment across annotated cell states at E9.5. Dot sizes indicate the fraction of gene-expressing cells in percentage within the annotated cell states across all analyzed sections. Color scale in the legend indicates mean expression levels within each group normalized per gene.

(F) Bar plot indicating the absolute number of detected cells with microglia progenitor signature across annotated cell states at E9.5. Cell states are sorted by microglia progenitor abundance.

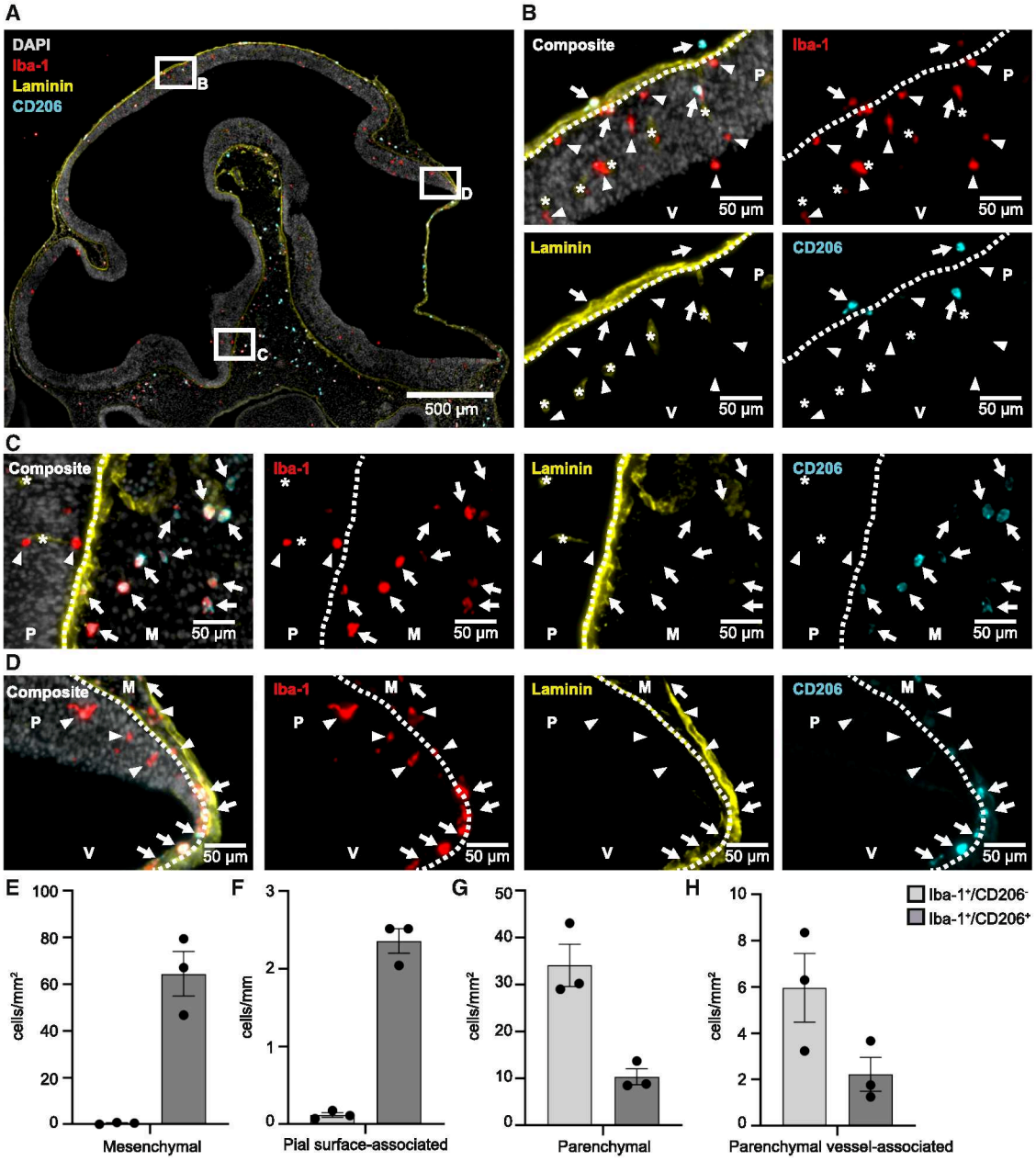


Figure 6. Migrating Iba-1$^+$CD206$^+$ microglia progenitors associate with ECM at the pial surface during CNS colonization

(A–D) (A) Representative immunofluorescent image of the head region at E10.5. Iba-1 (red), laminin (yellow), CD206 (cyan), and DAPI (white) are shown. Scale bar, 500 µm. Zoom-ins shown in (B)–(D) are indicated with white boxes. (B–D) Representative immunofluorescent images of different head regions, as indicated in (A). Scale bar, 50 µm. Separate antibody channels are shown. Arrowheads indicate Iba-1$^+$CD206$^+$ cells, arrows mark Iba-1$^+$CD206$^-$ cells, and asterisks denote vessels lacking intraluminal progenitors. P, parenchyma; V, ventricle; M, mesenchyme. One representative embryo out of three is shown.

(E–H) Quantification of Iba-1$^+$CD206$^-$ cells ($n = 3$) and Iba-1$^+$CD206$^+$ cells ($n = 3$) at E10.5 in the head mesenchyme (E), pial surface (F), brain parenchyma (G), and (H) associated with vessel structures in the brain parenchyma. Mean ± SEM is shown. Dots represent individual animals.

around E9.5.[9,10,19] However, migration of microglia progenitors into the embryonic CNS until E13.5–E15.5 was described, with a recent publication highlighting the contribution of macrophage progenitors to embryonic microglia in the pallium via the ventricular system at E12.5,[21] though molecular factors guiding this process remain unknown. Our study focused on the initial migration process of microglia progenitors into the CNS around E9.5. YS progenitors enter the embryo via circulation between E8.5 and E10.5.[22] The early CNS colonization has also been linked to developing vasculature, as *Ncx1*-deficient mice show reduced microglia,[9] but vessel-independent routes have also been proposed.[8,10] Our data support a migration from the pial surface into the parenchyma. Within our experimental approaches, we found no evidence of vascular extravasation of

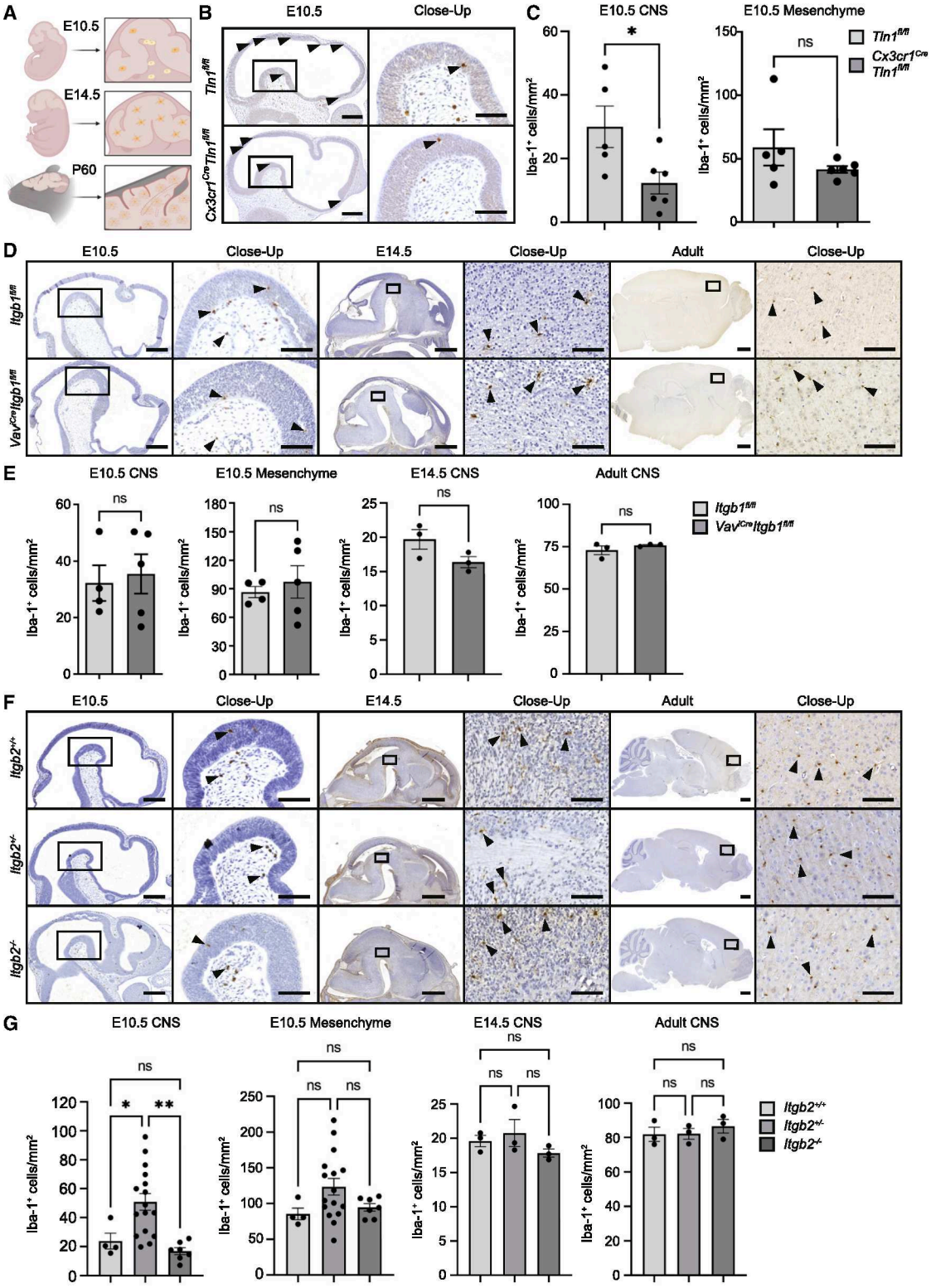


Figure 7. Microglia colonization of the developing CNS is dependent on Tln1

(A) Workflow of histological analysis of Iba-1 stained sections at E10.5, E14.5, and P60. Created in BioRender: Kierdorf, K. (2025) https://BioRender.com/0bmu097.

(B) Representative images of *Tln1*$^{fl/fl}$ (upper row) and *Cx3cr1*^{Cre}*Tln1*$^{fl/fl}$ (lower row) embryos at E10.5. Overview scale bar, 250 μm; close-up scale bar, 100 μm.

(legend continued on next page)

microglia, and many microglia are already present in the forebrain at E10.5, before local vascularization begins.[34] In the adult, leukocyte extravasation from the vasculature into inflamed tissue is integrin-dependent; however, we did not find evidence that colonization of the head mesenchyme from the YS is affected by *Tln1* or *Itgb2* deficiency. Interestingly, we found microglia as early as E10.5 to be associated with developing vasculature in the parenchyma, maybe reflecting their previously described role as Tip-macrophages involved in guiding vascular development.[35]

In line with our results, CD206^{+} progenitors have been previously described at the pial surface of the CNS during early development, which were assumed to be direct progenitors of CAMs, whereas microglia progenitors were suggested to be CD206^{-}.[19] We recently demonstrated that also embryonic microglia are derived from these CD206^{+} progenitors and downregulate CD206 as soon as they enter the CNS.[20] We confirmed that most progenitors at the pial surface and in the mesenchyme express CD206, which is rapidly lost upon CNS entry. Our scRNA-seq analyses highlighted a unique migratory profile of *Mrc1*$^{+}$ progenitors in the YS and embryo and a sequential appearance of *Mrc1*$^{+}$ progenitors followed by *Mrc1*$^{-}$ progenitors in the embryo. Overall, our data and existing literature support a stepwise migration process, where YS progenitors colonize the embryo via the blood stream followed by a mesenchyme-to-CNS migration of CD206^{+} microglia progenitors, which give rise to CD206^{-} embryonic microglia in the CNS parenchyma.

Our scRNA-seq analysis of YS progenitors pointed to an induction of adhesion molecules, including integrins, and a potential role in CNS colonization. We found a dynamic regulation of integrins on microglia throughout development. It has been described before that integrins, such as $\alpha_x\beta_2$ or $\alpha_5\beta_1$, are tightly controlled during microglia development. White matter-associated microglia involved in oligodendrogenesis express high levels of $\alpha_x\beta_2$.[41] Between E13.5 and E17.5, embryonic microglia express high levels of $\alpha_5\beta_1$, and their migration into the cortex depends on $\alpha_5\beta_1$-fibronectin interaction.[42] Consistent with these previous studies, our data showed that microglial integrin profiles change over development, with constitutive expression of $\alpha_M\beta_2$ and dynamic upregulation of $\alpha_L\beta_2$ and $\alpha_4\beta_1$ peaking during initial CNS colonization. These integrin expression changes may reflect developmental stage-specific microglial functions like phagocytosis, migration, or expansion, and may also influence microglia network formation and morphology, as shown for meningeal mast cells.[43]

Recently, we described that perivascular macrophages employ integrins to invade the opening perivascular space postnatally.[20] We reported before that microglia cell number at E14.5 is not affected by loss of high-affinity integrin binding in *Cx3cr1*^{Cre}*Tln1*$^{fl/fl}$ mice. By contrast, we now provide additional evidence that the initial colonization of the CNS by microglia progenitors is dependent on high-affinity integrin binding, whereas *Tln1*-deficient microglia progenitors showed a reduced capacity to colonize the developing CNS from the pial surface. From our data, we can speculate that reduced infiltration of microglia progenitors in *Cx3cr1*^{Cre}*Tln1*$^{fl/fl}$ mice will result in an increased proliferation of embryonic microglia, normalizing microglia cell numbers in later development. An effect also observed after induced depletion of embryonic microglia by Csf1r inhibitor treatment during development.[19,44,45]

We tested the effects of *Itgb1* and *Itgb2* deficiency on the recruitment of microglia progenitors to the developing CNS but did not find effects on the initial migration process nor in later developmental time points. In adult mice, we reported before that *Itgb2* deficiency did not affect Kupffer cell number in the liver or red pulp macrophages in the spleen, which are also derived from YS progenitors.[37]

Surprisingly, we found an increased number of microglia in the CNS of *Itgb2*$^{+/-}$ embryos at E10.5. We hypothesize that reduced adhesion at the pial surface accelerates microglia progenitor migration, as cell migration speed peaks at intermediate adhesion between cell and substrate. This balance is regulated by substrate or ECM availability and surface integrin expression.[46,47] Potential host tissue cells facilitating the entrance of microglia in the developing CNS could be mesenchymal progenitor cells located at the pial surface within the developing leptomeninges.[48]

Macrophage progenitors colonizing the head mesenchyme are not affected by deficiency or haploinsufficiency for *Itgb2*, which could indicate that they enter or distribute in an integrin-independent process in the mesenchyme. Future investigations should examine whether integrin profiles differ between tissue-resident macrophage populations and their progenitors and

(C) Quantification of Iba-1^{+} cells at E10.5 inside the CNS (left) and in the head mesenchyme (right) of *Tln1*$^{fl/fl}$ ($n = 6$) and *Cx3cr1*^{Cre}*Tln1*$^{fl/fl}$ embryos ($n = 5$). Mean ± SEM is shown, and dots represent individual animals. Unpaired t test: ns, not significant, $^{*}p < 0.05$.

(D) Representative images of *Itgb1*$^{fl/fl}$ (upper row) and *Vav*^{iCre}*Itgb1*$^{fl/fl}$ (lower row) embryos at E10.5 (left), E14.5 (middle), and P60 (right). Overview scale bar, 250 μm (E10.5), 500 μm (E14.5), 1,000 μm (P60), close-up scale bar, 100 μm (E10.5, E14.5, and P60).

(E) Quantification of Iba-1^{+} cells at E10.5 inside the CNS (left) and in the head mesenchyme (middle left) of *Itgb1*$^{fl/fl}$ ($n = 4$) and *Vav*^{iCre}*Itgb1*$^{fl/fl}$ embryos ($n = 5$). Mean ± SEM is shown, and dots represent individual animals. Unpaired t test: ns, not significant. Quantification of Iba-1^{+} cells at E14.5 inside the CNS (middle right) of *Itgb1*$^{fl/fl}$ ($n = 3$) and *Vav*^{iCre}*Itgb1*$^{fl/fl}$ embryos ($n = 3$). Mean ± SEM is shown, and dots represent individual animals. Unpaired t test: ns, not significant. Quantification of cortical Iba-1^{+} cells at P60 (right) of *Itgb1*$^{fl/fl}$ ($n = 3$) and *Vav*^{iCre}*Itgb1*$^{fl/fl}$ mice ($n = 3$). Mean ± SEM is shown, and dots represent individual animals. Unpaired t test: ns, not significant.

(F) Representative images of *Itgb2*$^{+/+}$ (upper row), *Itgb2*$^{+/-}$ (middle row), and *Itgb2*$^{-/-}$ (lower row) embryos at E10.5 (left), E14.5 (middle), and P60 (right). Overview scale bar, 250 μm (E10.5), 500 μm (E14.5), 1,000 μm (P60), close-up scale bar, 100 μm (E10.5, E14.5, P60).

(G) Quantification of Iba-1^{+} cells at E10.5 inside the CNS (left) and in the head mesenchyme (middle left) of *Itgb2*$^{+/+}$ ($n = 4$), *Itgb2*$^{+/-}$ ($n = 16$), and *Itgb2*$^{-/-}$ ($n = 7$) embryos. Mean ± SEM is shown, and dots represent individual animals. One-way ANOVA with Tukey's multiple comparison test: ns, not significant, $^{*}p < 0.05$, $^{**}p < 0.01$. Quantification of Iba-1^{+} cells at E14.5 inside the CNS (middle right) of *Itgb2*$^{+/+}$ ($n = 3$), *Itgb2*$^{+/-}$ ($n = 3$), and *Itgb2*$^{-/-}$ embryos ($n = 3$). Mean ± SEM is shown, and dots represent individual animals. One-way ANOVA with Tukey's multiple comparison test: ns, not significant. Quantification of cortical Iba-1^{+} cells at P60 (right) of *Itgb2*$^{+/+}$ ($n = 3$), *Itgb2*$^{+/-}$ ($n = 3$), and *Itgb2*$^{-/-}$ mice ($n = 3$). Mean ± SEM is shown, and dots represent individual animals. One-way ANOVA with Tukey's multiple comparison test: ns, not significant.

whether their tissue migration is integrin dependent based on route, timing, and ontogeny. Furthermore, it remains to be defined which other factors contribute to the recruitment and guidance of microglia progenitors into the CNS as one of the first organs during development.

Limitations of the study

Despite our findings that *Tln1* deficiency results in reduced microglia migration into the CNS, we could not yet define which class of integrins is involved in this process. A potential explanation could be compensatory mechanisms between integrins,[49,50] as reported before for immune cell adhesion and migration.[51–54] Compensatory mechanisms may involve alternative integrin signaling, altered surface expression of other integrins, or both.[53] Future exploration of integrin compensation mechanisms could be highly relevant to further characterize microglia migration into the CNS. Specific substrates or binding partners for integrin-mediated migration of microglia progenitors from the pial surface into the CNS remain yet to be defined. Our study points to a mesenchyme-to-CNS migration of microglia progenitors; however, with our experimental approaches, we cannot exclude direct extravasation of microglia progenitors from vessels into the CNS parenchyma.

RESOURCE AVAILABILITY

Lead contact

Requests for further information and resources should be directed to and will be fulfilled by the lead contact, Katrin Kierdorf (katrin.kierdorf@uniklinik-freiburg.de).

Materials availability

This study did not generate new, unique reagents.

Data and code availability

- Bulk RNA sequencing data have been deposited at GEO: GSE249007 and are publicly available as of the date of publication. LC-MS/MS-based proteomics data have been deposited at the mass spectrometry interactive virtual environment (MassIVE) as MSV000097998 and are publicly available as of the date of publication. This paper analyzes existing, publicly available data, accessible at GEO: GSE195437, GSE119945, and GSE197353.
- This paper does not report original code.
- Any additional information required to reanalyze the data reported in this paper is available from the lead contact upon request.

ACKNOWLEDGMENTS

We thank Maria Oberle for excellent technical assistance and Reinhard Fässler for providing *Itgb1*$^{fl/fl}$ mice. Illumina sequencing was performed at the Genomics Core Unit Center of Excellence for Fluorescent Bioanalytics (KFB, University of Regensburg, Germany). K.K. was supported by the Fritz Thyssen Foundation and the DFG Heisenberg Program (Project-ID 544402801). K.K., M.P., T.L., M.B., L.A., and O.G. were funded by the DFG within TRR167 (Project-ID 259373024). K.K., M.P., O.G., and M.B. were supported by CRC1479 (Project-ID 441891347), CRC1160 (Project-ID 256073931), and Germany's Excellence Strategy (EXC-2189, Project-ID 390939984). K.K., M.P., and M.B. also received funding from TRR359 (Project-ID 491676693). T.L. was supported by TRR332 (Project-ID 449437943), CRC1450 (Project-ID 431460824), and the Max Planck Society. O.G. was funded through CRC1425 (Project-ID 422681845), GRK2606 (Project-ID 423813989), GRK2344 (Project-ID 322977937), ERC Starting Grant (337689), ERC Proof-of-Concept Grant (966687), and EU-H2020-MSCA-COFUND EURIdoc (101034170). M.P. received support from the Novo Nordisk Foundation, the Ernst Jung Foundation, and the Gottfried Wilhelm Leibniz Prize. M.B. was supported by CRC1453 (Project ID 431984000) and FOR5476 (Project ID 493802833). M.B. and G.A. received BMBF funding via MIRACUM (PM4Onco-FKZ 01ZZ2322A for M.B., EkoEstMed-FKZ 01ZZ2015 for G.A.). T.-L.J.D. was funded by DFG GRK2344 (MeInBio, Project-ID 322977937). S.M. and A.S. were supported by Germany's Excellence Strategy—EXC2151 (Project-ID 390873048). The graphical abstract was created in BioRender: Kierdorf, K. (2025) https://BioRender.com/i8vbhbf. Schemes of workflows were created in BioRender: Kierdorf, K. (2025) https://BioRender.com/0bmu097.

AUTHOR CONTRIBUTIONS

Conceptualization, K.K.; methodology, M.P., O.S., and K.K.; software, T.-L.J.D., O.S., R.S., and S.M.; formal analysis, P.P., A.O., R.S., M.B., G.A., T.-L.J.D., S.M., and A.S.; investigation, P.P., A.O., T.-L.J.D., H.B., L.A., and C.C.; resources, O.G., M.H., M.P., O.S., T.L., E.N., L.A., and N.P.; writing, P.P., A.O., and K.K.; visualization, P.P., A.O., S.M., and T.-L.J.D.; supervision, K.K.; project administration, K.K.; funding acquisition, K.K.

DECLARATION OF INTERESTS

O.G. is a co-inventor on patent applications for immunomodulators and a co-founder of EMUNO Therapeutics, a company developing drugs that control immunity to address unmet clinical needs. None of the drug candidates in patenting or development were used in this study.

STAR★METHODS

Detailed methods are provided in the online version of this paper and include the following:

- KEY RESOURCES TABLE
- EXPERIMENTAL MODEL AND STUDY PARTICIPANT DETAILS
  - Animals
- METHOD DETAILS
  - Timed matings
  - Dissection of embryos
  - Cardiac perfusion and dissection of adult brains
  - Cell isolation protocol for flow cytometry
  - Cell staining for flow cytometry and analysis
  - Chromogenic Immunohistochemistry
  - Immunofluorescence stainings and imaging
  - Liquid chromatography – tandem mass spectrometry (LC-MS/MS) analysis
  - Bulk RNA-sequencing
  - Bulk RNA-sequencing analysis
  - Single cell RNA-sequencing of yolk sac progenitors and analysis
  - Analysis of spatial transcriptomic and scRNA-seq data set of whole mouse embryos
- QUANTIFICATION AND STATISTICAL ANALYSIS

SUPPLEMENTAL INFORMATION

Supplemental information can be found online at https://doi.org/10.1016/j.devcel.2025.08.012.

Received: July 30, 2024
Revised: March 31, 2025
Accepted: August 18, 2025
Published: September 10, 2025

REFERENCES

1. Ginhoux, F., and Guilliams, M. (2016). Tissue-Resident Macrophage Ontogeny and Homeostasis. Immunity *44*, 439–449. https://doi.org/10.1016/j.immuni.2016.02.024.

CellPress
OPEN ACCESS

2. Mass, E., Nimmerjahn, F., Kierdorf, K., and Schlitzer, A. (2023). Tissue-specific macrophages: how they develop and choreograph tissue biology. Nat. Rev. Immunol. *23*, 563–579. https://doi.org/10.1038/s41577-023-00848-y.

3. Prinz, M., Masuda, T., Wheeler, M.A., and Quintana, F.J. (2021). Microglia and Central Nervous System-Associated Macrophages-From Origin to Disease Modulation. Annu. Rev. Immunol. *39*, 251–277. https://doi.org/10.1146/annurev-immunol-093019-110159.

4. Goldmann, T., Wieghofer, P., Jordão, M.J.C., Prutek, F., Hagemeyer, N., Frenzel, K., Amann, L., Staszewski, O., Kierdorf, K., Krueger, M., et al. (2016). Origin, fate and dynamics of macrophages at central nervous system interfaces. Nat. Immunol. *17*, 797–805. https://doi.org/10.1038/ni.3423.

5. Van Hove, H., Martens, L., Scheyltjens, I., De Vlaminck, K., Pombo Antunes, A.R., De Prijck, S., Vandamme, N., De Schepper, S., Van Isterdael, G., Scott, C.L., et al. (2019). A single-cell atlas of mouse brain macrophages reveals unique transcriptional identities shaped by ontogeny and tissue environment. Nat. Neurosci. *22*, 1021–1035. https://doi.org/10.1038/s41593-019-0393-4.

6. Sankowski, R., Süß, P., Benkendorff, A., Böttcher, C., Fernandez-Zapata, C., Chhatbar, C., Cahueau, J., Monaco, G., Gasull, A.D., Khavaran, A., et al. (2024). Multiomic spatial landscape of innate immune cells at human central nervous system borders. Nat. Med. *30*, 186–198. https://doi.org/10.1038/s41591-023-02673-1.

7. Amann, L., Fell, A., Monaco, G., Sankowski, R., Wu, H.Z.Q., Jordão, M.J.C., Borst, K., Fliegauf, M., Masuda, T., Ardura-Fabregat, A., et al. (2024). Extrasinusoidal macrophages are a distinct subset of immunologically active dural macrophages. Sci. Immunol. *9*, eadh1129. https://doi.org/10.1126/sciimmunol.adh1129.

8. Alliot, F., Godin, I., and Pessac, B. (1999). Microglia derive from progenitors, originating from the yolk sac, and which proliferate in the brain. Brain Res. Dev. Brain Res. *117*, 145–152. https://doi.org/10.1016/s0165-3806(99)00113-3.

9. Ginhoux, F., Greter, M., Leboeuf, M., Nandi, S., See, P., Gokhan, S., Mehler, M.F., Conway, S.J., Ng, L.G., Stanley, E.R., et al. (2010). Fate mapping analysis reveals that adult microglia derive from primitive macrophages. Science *330*, 841–845. https://doi.org/10.1126/science.1194637.

10. Kierdorf, K., Erny, D., Goldmann, T., Sander, V., Schulz, C., Perdiguero, E.G., Wieghofer, P., Heinrich, A., Riemke, P., Hölscher, C., et al. (2013). Microglia emerge from erythromyeloid precursors via Pu.1- and Irf8-dependent pathways. Nat. Neurosci. *16*, 273–280. https://doi.org/10.1038/nn.3318.

11. Hammond, T.R., Dufort, C., Dissing-Olesen, L., Giera, S., Young, A., Wysoker, A., Walker, A.J., Gergits, F., Segel, M., Nemesh, J., et al. (2019). Single-Cell RNA Sequencing of Microglia throughout the Mouse Lifespan and in the Injured Brain Reveals Complex Cell-State Changes. Immunity *50*, 253–271.e6. https://doi.org/10.1016/j.immuni.2018.11.004.

12. Li, Q., Cheng, Z., Zhou, L., Darmanis, S., Neff, N.F., Okamoto, J., Gulati, G., Bennett, M.L., Sun, L.O., Clarke, L.E., et al. (2019). Developmental Heterogeneity of Microglia and Brain Myeloid Cells Revealed by Deep Single-Cell RNA Sequencing. Neuron *101*, 207–223.e10. https://doi.org/10.1016/j.neuron.2018.12.006.

13. Masuda, T., Sankowski, R., Staszewski, O., Böttcher, C., Amann, L., Sagar, Scheiwe, C., Nessler, S., Kunz, P., van Loo, G., et al. (2019). Spatial and temporal heterogeneity of mouse and human microglia at single-cell resolution. Nature *566*, 388–392. https://doi.org/10.1038/s41586-019-0924-x.

14. Gomez Perdiguero, E., Klapproth, K., Schulz, C., Busch, K., Azzoni, E., Crozet, L., Garner, H., Trouillet, C., de Bruijn, M.F., Geissmann, F., et al. (2015). Tissue-resident macrophages originate from yolk-sac-derived erythro-myeloid progenitors. Nature *518*, 547–551. https://doi.org/10.1038/nature13989.

15. Kasaai, B., Caolo, V., Peacock, H.M., Lehoux, S., Gomez-Perdiguero, E., Luttun, A., and Jones, E.A.V. (2017). Erythro-myeloid progenitors can differentiate from endothelial cells and modulate embryonic vascular remodeling. Sci. Rep. *7*, 43817. https://doi.org/10.1038/srep43817.

16. Bertrand, J.Y., Jalil, A., Klaine, M., Jung, S., Cumano, A., and Godin, I. (2005). Three pathways to mature macrophages in the early mouse yolk sac. Blood *106*, 3004–3011. https://doi.org/10.1182/blood-2005-02-0461.

17. Mass, E., Ballesteros, I., Farlik, M., Halbritter, F., Günther, P., Crozet, L., Jacome-Galarza, C.E., Händler, K., Klughammer, J., Kobayashi, Y., et al. (2016). Specification of tissue-resident macrophages during organogenesis. Science *353*, aaf4238. https://doi.org/10.1126/science.aaf4238.

18. Hagemeyer, N., Kierdorf, K., Frenzel, K., Xue, J., Ringelhan, M., Abdullah, Z., Godin, I., Wieghofer, P., Costa Jordão, M.J., Ulas, T., et al. (2016). Transcriptome-based profiling of yolk sac-derived macrophages reveals a role for Irf8 in macrophage maturation. EMBO J. *35*, 1730–1744. https://doi.org/10.15252/embj.201693801.

19. Utz, S.G., See, P., Mildenberger, W., Thion, M.S., Silvin, A., Lutz, M., Ingelfinger, F., Rayan, N.A., Lelios, I., Buttgereit, A., et al. (2020). Early Fate Defines Microglia and Non-parenchymal Brain Macrophage Development. Cell *181*, 557–573.e18. https://doi.org/10.1016/j.cell.2020.03.021.

20. Masuda, T., Amann, L., Monaco, G., Sankowski, R., Staszewski, O., Krueger, M., Del Gaudio, F., He, L., Paterson, N., Nent, E., et al. (2022). Specification of CNS macrophage subsets occurs postnatally in defined niches. Nature *604*, 740–748. https://doi.org/10.1038/s41586-022-04596-2.

21. Hattori, Y., Kato, D., Murayama, F., Koike, S., Asai, H., Yamasaki, A., Naito, Y., Kawaguchi, A., Konishi, H., Prinz, M., et al. (2023). CD206+ macrophages transventricularly infiltrate the early embryonic cerebral wall to differentiate into microglia. Cell Rep. *42*, 112092. https://doi.org/10.1016/j.celrep.2023.112092.

22. Stremmel, C., Schuchert, R., Wagner, F., Thaler, R., Weinberger, T., Pick, R., Mass, E., Ishikawa-Ankerhold, H.C., Margraf, A., Hutter, S., et al. (2018). Yolk sac macrophage progenitors traffic to the embryo during defined stages of development. Nat. Commun. *9*, 75. https://doi.org/10.1038/s41467-017-02492-2.

23. Wu, S., Xue, R., Hassan, S., Nguyen, T.M.L., Wang, T., Pan, H., Xu, J., Liu, Q., Zhang, W., and Wen, Z. (2018). Il34-Csf1r Pathway Regulates the Migration and Colonization of Microglial Precursors. Dev. Cell *46*, 552–563.e4. https://doi.org/10.1016/j.devcel.2018.08.005.

24. Casano, A.M., Albert, M., and Peri, F. (2016). Developmental Apoptosis Mediates Entry and Positioning of Microglia in the Zebrafish Brain. Cell Rep. *16*, 897–906. https://doi.org/10.1016/j.celrep.2016.06.033.

25. Xu, J., Wang, T., Wu, Y., Jin, W., and Wen, Z. (2016). Microglia Colonization of Developing Zebrafish Midbrain Is Promoted by Apoptotic Neuron and Lysophosphatidylcholine. Dev. Cell *38*, 214–222. https://doi.org/10.1016/j.devcel.2016.06.018.

26. Tirosh, I., Izar, B., Prakadan, S.M., Wadsworth, M.H., Treacy, D., Trombetta, J.J., Rotem, A., Rodman, C., Lian, C., Murphy, G., et al. (2016). Dissecting the multicellular ecosystem of metastatic melanoma by single-cell RNA-seq. Science *352*, 189–196. https://doi.org/10.1126/science.aad0501.

27. Chastney, M.R., Conway, J.R.W., and Ivaska, J. (2021). Integrin adhesion complexes. Curr. Biol. *31*, R536–R542. https://doi.org/10.1016/j.cub.2021.01.038.

28. Cao, J., Spielmann, M., Qiu, X., Huang, X., Ibrahim, D.M., Hill, A.J., Zhang, F., Mundlos, S., Christiansen, L., Steemers, F.J., et al. (2019). The single-cell transcriptional landscape of mammalian organogenesis. Nature *566*, 496–502. https://doi.org/10.1038/s41586-019-0969-x.

29. Dann, E., Henderson, N.C., Teichmann, S.A., Morgan, M.D., and Marioni, J.C. (2022). Differential abundance testing on single-cell data using k-nearest neighbor graphs. Nat. Biotechnol. *40*, 245–253. https://doi.org/10.1038/s41587-021-01033-z.

30. Efremova, M., Vento-Tormo, M., Teichmann, S.A., and Vento-Tormo, R. (2020). CellPhoneDB: inferring cell-cell communication from combined expression of multi-subunit ligand-receptor complexes. Nat. Protoc. *15*, 1484–1506. https://doi.org/10.1038/s41596-020-0292-x.

31. Naba, A., Clauser, K.R., Hoersch, S., Liu, H., Carr, S.A., and Hynes, R.O. (2012). The matrisome: in silico definition and in vivo characterization by proteomics of normal and tumor extracellular matrices. Mol. Cell. Proteomics *11*, M111.014647. https://doi.org/10.1074/mcp.M111.014647.

32. Naba, A., Clauser, K.R., Ding, H., Whittaker, C.A., Carr, S.A., and Hynes, R. O. (2016). The extracellular matrix: Tools and insights for the "omics" era. Matrix Biol. *49*, 10–24. https://doi.org/10.1016/j.matbio.2015.06.003.

33. Sampath Kumar, A., Tian, L., Bolondi, A., Hernández, A.A., Stickels, R., Kretzmer, H., Murray, E., Wittler, L., Walther, M., Barakat, G., et al. (2023). Spatiotemporal transcriptomic maps of whole mouse embryos at the onset of organogenesis. Nat. Genet. *55*, 1176–1185. https://doi.org/10.1038/s41588-023-01435-6.

34. Tata, M., Ruhrberg, C., and Fantin, A. (2015). Vascularisation of the central nervous system. Mech. Dev. *138*, 26–36. https://doi.org/10.1016/j.mod.2015.07.001.

35. Fantin, A., Vieira, J.M., Gestri, G., Denti, L., Schwarz, Q., Prykhozhij, S., Peri, F., Wilson, S.W., and Ruhrberg, C. (2010). Tissue macrophages act as cellular chaperones for vascular anastomosis downstream of VEGF-mediated endothelial tip cell induction. Blood *116*, 829–840. https://doi.org/10.1182/blood-2009-12-257832.

36. Wiesner, C., Le-Cabec, V., El Azzouzi, K., Maridonneau-Parini, I., and Linder, S. (2014). Podosomes in space: macrophage migration and matrix degradation in 2D and 3D settings. Cell Adh. Migr. *8*, 179–191. https://doi.org/10.4161/cam.28116.

37. Paterson, N., and Lämmermann, T. (2022). Macrophage network dynamics depend on haptokinesis for optimal local surveillance. eLife *11*, e75354. https://doi.org/10.7554/eLife.75354.

38. Lämmermann, T., and Sixt, M. (2009). Mechanical modes of 'amoeboid' cell migration. Curr. Opin. Cell Biol. *21*, 636–644. https://doi.org/10.1016/j.ceb.2009.05.003.

39. Lu, F., Zhu, L., Bromberger, T., Yang, J., Yang, Q., Liu, J., Plow, E.F., Moser, M., and Qin, J. (2022). Mechanism of integrin activation by talin and its cooperation with kindlin. Nat. Commun. *13*, 2362. https://doi.org/10.1038/s41467-022-30117-w.

40. Zhu, L., Yang, J., Bromberger, T., Holly, A., Lu, F., Liu, H., Sun, K., Klapproth, S., Hirbawi, J., Byzova, T.V., et al. (2017). Structure of Rap1b bound to talin reveals a pathway for triggering integrin activation. Nat. Commun. *8*, 1744. https://doi.org/10.1038/s41467-017-01822-8.

41. Hagemeyer, N., Hanft, K.-M., Akriditou, M.-A., Unger, N., Park, E.S., Stanley, E.R., Staszewski, O., Dimou, L., and Prinz, M. (2017). Microglia contribute to normal myelinogenesis and to oligodendrocyte progenitor maintenance during adulthood. Acta Neuropathol. *134*, 441–458. https://doi.org/10.1007/s00401-017-1747-1.

42. Smolders, S.M.-T., Swinnen, N., Kessels, S., Arnauts, K., Smolders, S., Le Bras, B., Rigo, J.-M., Legendre, P., and Brône, B. (2017). Age-specific function of α5β1 integrin in microglial migration during early colonization of the developing mouse cortex. Glia *65*, 1072–1088. https://doi.org/10.1002/glia.23145.

43. Kaltenbach, L., Martzloff, P., Bambach, S.K., Aizarani, N., Mihlan, M., Gavrilov, A., Glaser, K.M., Stecher, M., Thünauer, R., Thiriot, A., et al. (2023). Slow integrin-dependent migration organizes networks of tissue-resident mast cells. Nat. Immunol. *24*, 915–924. https://doi.org/10.1038/s41590-023-01493-2.

44. Rosin, J.M., Vora, S.R., and Kurrasch, D.M. (2018). Depletion of embryonic microglia using the CSF1R inhibitor PLX5622 has adverse sex-specific effects on mice, including accelerated weight gain, hyperactivity and anxiolytic-like behaviour. Brain Behav. Immun. *73*, 682–697. https://doi.org/10.1016/j.bbi.2018.07.023.

45. Lawrence, A.R., Canzi, A., Bridlance, C., Olivié, N., Lansonneur, C., Catale, C., Pizzamiglio, L., Kloeckner, B., Silvin, A., Munro, D.A.D., et al. (2024). Microglia maintain structural integrity during fetal brain morphogenesis. Cell *187*, 962–980.e19. https://doi.org/10.1016/j.cell.2024.01.012.

46. Gupton, S.L., and Waterman-Storer, C.M. (2006). Spatiotemporal Feedback between Actomyosin and Focal-Adhesion Systems Optimizes Rapid Cell Migration. Cell *125*, 1361–1374. https://doi.org/10.1016/j.cell.2006.05.029.

47. Palecek, S.P., Loftus, J.C., Ginsberg, M.H., Lauffenburger, D.A., and Horwitz, A.F. (1997). Integrin-ligand binding properties govern cell migration speed through cell-substratum adhesiveness. Nature *385*, 537–540. https://doi.org/10.1038/385537a0.

48. Dasgupta, K., and Jeong, J. (2019). Developmental Biology of the Meninges. Genesis *57*, e23288. https://doi.org/10.1002/dvg.23288.

49. Morrison, V.L., James, M.J., Grzes, K., Cook, P., Glass, D.G., Savinko, T., Lek, H.S., Gawden-Bone, C., Watts, C., Millington, O.R., et al. (2014). Loss of beta2-integrin-mediated cytoskeletal linkage reprogrammes dendritic cells to a mature migratory phenotype. Nat. Commun. *5*, 5359. https://doi.org/10.1038/ncomms6359.

50. Bouvard, D., Brakebusch, C., Gustafsson, E., Aszódi, A., Bengtsson, T., Berna, A., and Fässler, R. (2001). Functional Consequences of Integrin Gene Mutations in Mice. Circ. Res. *89*, 211–223. https://doi.org/10.1161/hh1501.094874.

51. Schläger, C., Körner, H., Krueger, M., Vidoli, S., Haberl, M., Mielke, D., Brylla, E., Issekutz, T., Cabañas, C., Nelson, P.J., et al. (2016). Effector T-cell trafficking between the leptomeninges and the cerebrospinal fluid. Nature *530*, 349–353. https://doi.org/10.1038/nature16939.

52. Glatigny, S., Duhen, R., Arbelaez, C., Kumari, S., and Bettelli, E. (2015). Integrin alpha L controls the homing of regulatory T cells during CNS autoimmunity in the absence of integrin alpha 4. Sci. Rep. *5*, 7834. https://doi.org/10.1038/srep07834.

53. Walling, B.L., and Kim, M. (2018). LFA-1 in T Cell Migration and Differentiation. Front. Immunol. *9*, 952. https://doi.org/10.3389/fimmu.2018.00952.

54. Overstreet, M.G., Gaylo, A., Angermann, B.R., Hughson, A., Hyun, Y.-M., Lambert, K., Acharya, M., Billroth-Maclurg, A.C., Rosenberg, A.F., Topham, D.J., et al. (2013). Inflammation-induced interstitial migration of effector $CD4^+$ T cells is dependent on integrin αV. Nat. Immunol. *14*, 949–958. https://doi.org/10.1038/ni.2682.

55. Scharffetter-Kochanek, K., Lu, H., Norman, K., van Nood, N., Munoz, F., Grabbe, S., McArthur, M., Lorenzo, I., Kaplan, S., Ley, K., et al. (1998). Spontaneous skin ulceration and defective T cell function in CD18 null mice. J. Exp. Med. *188*, 119–131. https://doi.org/10.1084/jem.188.1.119.

56. Yona, S., Kim, K.-W., Wolf, Y., Mildner, A., Varol, D., Breker, M., Strauss-Ayali, D., Viukov, S., Guilliams, M., Misharin, A., et al. (2013). Fate mapping reveals origins and dynamics of monocytes and tissue macrophages under homeostasis. Immunity *38*, 79–91. https://doi.org/10.1016/j.immuni.2012.12.001.

57. Goldmann, T., Wieghofer, P., Müller, P.F., Wolf, Y., Varol, D., Yona, S., Brendecke, S.M., Kierdorf, K., Staszewski, O., Datta, M., et al. (2013). A new type of microglia gene targeting shows TAK1 to be pivotal in CNS autoimmune inflammation. Nat. Neurosci. *16*, 1618–1626. https://doi.org/10.1038/nn.3531.

58. de Boer, J., Williams, A., Skavdis, G., Harker, N., Coles, M., Tolaini, M., Norton, T., Williams, K., Roderick, K., Potocnik, A.J., et al. (2003). Transgenic mice with hematopoietic and lymphoid specific expression of Cre. Eur. J. Immunol. *33*, 314–325. https://doi.org/10.1002/immu.200310005.

59. Nieswandt, B., Moser, M., Pleines, I., Varga-Szabo, D., Monkley, S., Critchley, D., and Fässler, R. (2007). Loss of talin1 in platelets abrogates integrin activation, platelet aggregation, and thrombus formation in vitro and in vivo. J. Exp. Med. *204*, 3113–3118. https://doi.org/10.1084/jem.20071827.

60. Potocnik, A.J., Brakebusch, C., and Fässler, R. (2000). Fetal and adult hematopoietic stem cells require beta1 integrin function for colonizing fetal liver, spleen, and bone marrow. Immunity *12*, 653–663. https://doi.org/10.1016/s1074-7613(00)80216-2.

61. Srinivas, S., Watanabe, T., Lin, C.S., William, C.M., Tanabe, Y., Jessell, T. M., and Costantini, F. (2001). Cre reporter strains produced by targeted insertion of EYFP and ECFP into the ROSA26 locus. BMC Dev. Biol. *1*, 4. https://doi.org/10.1186/1471-213x-1-4.

62. Theiler, K. (1972). The House Mouse. Development and Normal Stages from Fertilization to 4 Weeks of Age (Springer).

63. McClelland, K.S., Ng, E.T., and Bowles, J. (2016). Agarose/gelatin immobilisation of tissues or embryo segments for orientated paraffin embedding

and sectioning. Differentiation *91*, 68–71. https://doi.org/10.1016/j.diff.2015.12.001.

64. Baumert, H.M., Metzger, E., Fahrner, M., George, J., Thomas, R.K., Schilling, O., and Schüle, R. (2020). Depletion of histone methyltransferase KMT9 inhibits lung cancer cell proliferation by inducing non-apoptotic cell death. Cancer Cell Int. *20*, 52. https://doi.org/10.1186/s12935-020-1141-2.
65. Alexa, A., and Rahnenfuhrer, J. (2016). topGO: Enrichment Analysis for Gene Ontology. R package version 2240. https://bioconductor.org/packages/release/bioc/manuals/topGO/man/topGO.pdf.
66. Bolger, A.M., Lohse, M., and Usadel, B. (2014). Trimmomatic: a flexible trimmer for Illumina sequence data. Bioinformatics *30*, 2114–2120. https://doi.org/10.1093/bioinformatics/btu170.
67. Dobin, A., Davis, C.A., Schlesinger, F., Drenkow, J., Zaleski, C., Jha, S., Batut, P., Chaisson, M., and Gingeras, T.R. (2013). STAR: ultrafast universal RNA-seq aligner. Bioinformatics *29*, 15–21. https://doi.org/10.1093/bioinformatics/bts635.
68. Ritchie, M.E., Phipson, B., Wu, D., Hu, Y., Law, C.W., Shi, W., and Smyth, G.K. (2015). limma powers differential expression analyses for RNA-sequencing and microarray studies. Nucleic Acids Res. *43*, e47. https://doi.org/10.1093/nar/gkv007.
69. Subramanian, A., Tamayo, P., Mootha, V.K., Mukherjee, S., Ebert, B.L., Gillette, M.A., Paulovich, A., Pomeroy, S.L., Golub, T.R., Lander, E.S., et al. (2005). Gene set enrichment analysis: A knowledge-based approach for interpreting genome-wide expression profiles. Proc. Natl. Acad. Sci. USA *102*, 15545–15550. https://doi.org/10.1073/pnas.0506580102.
70. Wu, T., Hu, E., Xu, S., Chen, M., Guo, P., Dai, Z., Feng, T., Zhou, L., Tang, W., Zhan, L., et al. (2021). clusterProfiler 4.0: A universal enrichment tool for interpreting omics data. Innovation (Camb) *2*, 100141. https://doi.org/10.1016/j.xinn.2021.100141.
71. Yu, G., Wang, L.-G., Han, Y., and He, Q.-Y. (2012). clusterProfiler: an R package for comparing biological themes among gene clusters. Omics *16*, 284–287. https://doi.org/10.1089/omi.2011.0118.
72. Virshup, I., Bredikhin, D., Heumos, L., Palla, G., Sturm, G., Gayoso, A., Kats, I., Koutrouli, M., Scverse Community, Berger, B., and et al.. (2023). The scverse project provides a computational ecosystem for single-cell omics data analysis. Nat. Biotechnol. *41*, 604–606. https://doi.org/10.1038/s41587-023-01733-8.
73. Wolf, F.A., Angerer, P., and Theis, F.J. (2018). SCANPY: large-scale single-cell gene expression data analysis. Genome Biol. *19*, 15. https://doi.org/10.1186/s13059-017-1382-0.
74. Traag, V.A., Waltman, L., and van Eck, N.J. (2019). From Louvain to Leiden: guaranteeing well-connected communities. Sci. Rep. *9*, 5233. https://doi.org/10.1038/s41598-019-41695-z.
75. Heumos, L., Ji, Y., May, L., Green, T., Zhang, X., Wu, X., Ostner, J., Peidli, S., Schumacher, A., Hrovatin, K., et al. (2024). Pertpy: an end-to-end framework for perturbation analysis. Preprint at bioRxiv. https://doi.org/10.1101/2024.08.04.606516.
76. Dimitrov, D., Türei, D., Garrido-Rodriguez, M., Burmedi, P.L., Nagai, J.S., Boys, C., Ramirez Flores, R.O., Kim, H., Szalai, B., Costa, I.G., et al. (2022). Comparison of methods and resources for cell-cell communication inference from single-cell RNA-Seq data. Nat. Commun. *13*, 3224. https://doi.org/10.1038/s41467-022-30755-0.

STAR★METHODS

KEY RESOURCES TABLE

REAGENT or RESOURCE	SOURCE	IDENTIFIER
Antibodies		
Armenian Hamster monoclonal anti-mouse CD49b PE (clone HMalpha2)	BD Biosciences	Cat# 558759; RRID:AB_397108
Rat monoclonal anti-mouse CD41a PE (clone eBioMWReg30)	EBioscience	Cat# 12-0411-81; RRID:AB_763488
Rat monoclonal anti-mouse CD49d PE (clone R1-2)	eBioscience	Cat# 12-0492-82; RRID:AB_465697
Monoclonal anti-mouse CD49e PE (clone eBioHMa5-1)	eBioscience	Cat# 12-0493-83; RRID:AB_763505
Rat monoclonal anti-human/mouse CD49f PE (clone GoH3)	BioLegend	Cat# 313611; RRID:AB_893374
Rat monoclonal anti-mouse CD11a PE (clone M17/4)	eBioscience	Cat# 12-0111-82; RRID:AB_465544
Rat monoclonal anti-mouse CD51 PE (clone RMV-7)	eBioscience	Cat# 12-0512-82; RRID:AB_465704
Armenian Hamster monoclonal anti-mouse CD11c PE (clone N418)	eBioscience	Cat# 12-0114-82; RRID:AB_465552
Armenian Hamster monoclonal anti-mouse CD103 PE (clone 2E7)	eBioscience	Cat# 12-1031-81; RRID:AB_465798
Armenian Hamster monoclonal anti-mouse CD29 PE (clone eBioHMb1-1)	eBioscience	Cat# 12-0291-81; RRID:AB_657733
Rat monoclonal anti-mouse CD18 PE (clone C71/16)	BD Biosciences	Cat# 553293; RRID:AB_394762
Armenian Hamster monoclonal anti-mouse CD61 PE (clone 2C9.G3)	eBioscience	Cat# 12-0611-82; RRID:AB_465718
Rat monoclonal anti-mouse CD104 PE (clone 346-11A)	BioLegend	Cat# 123609; RRID:AB_2563543
Mouse monoclonal anti-mouse Integrin beta 5 PE (clone KN52)	eBioscience	Cat# 12-0497-73; RRID:AB_657809
Rat monoclonal anti-mouse integrin beta 7 PE (clone FIB504)	eBioscience	Cat# 12-5867-73; RRID:AB_953642
Rat monoclonal anti-mouse CD45 APC (clone 30-F11)	eBioscience	Cat# 17-0451-82; RRID:AB_469392
Rat monoclonal anti-mouse CD45 APC-Cy7 (clone 30-F11)	BioLegend	Cat# 103115; RRID:AB_312980
Rat monoclonal anti-mouse F4/80 PE-Cy7 (clone BM8)	BioLegend	Cat# 123113; RRID:AB_893490
Rat monoclonal anti-mouse CD11b BV-605 (clone M1/70)	BioLegend	Cat# 101237; RRID:AB_11126744
Rat monoclonal anti-mouse CD117 APC-Cy7 (clone 2B8)	BioLegend	Cat# 105825; RRID:AB_1626280
Rat monoclonal anti-mouse CD3 BV-711 (clone 17A2)	BioLegend	Cat# 100241; RRID:AB_2563945
Rat monoclonal anti-mouse CD19 BV-711 (clone 6D5)	BioLegend	Cat# 115555; RRID:AB_2563945
Rat monoclonal anti-mouse Ly-6G and Ly-6C (clone RB6-8C5)	BD Biosciences	Cat# 563849; RRID:AB_2738450
Guinea pig monoclonal anti-Iba-1 (clone Gp311H9)	Synaptic Systems	Cat# 234 308; RRID: AB_2924932
Rabbit polyclonal anti-Laminin	Millipore	Cat# AB19012; RRID:AB_2133893

(*Continued on next page*)

CellPress
OPEN ACCESS

Continued

REAGENT or RESOURCE	SOURCE	IDENTIFIER
Rat monoclonal anti-CD206 (clone MR5D3)	BioRad	Cat# MCA2235XZ; RRID:AB_324449
Goat anti-guinea pig Alexa Fluor® 488	Invitrogen	Cat# A-11073; RRID:AB_2534117
Goat anti-rabbit Alexa Fluor® 568	Invitrogen	Cat# A-21069; RRID:AB_141416
Goat anti-rat Alexa Fluor® 647	Invitrogen	Cat# A-21247; RRID:AB_141778
Chemicals, peptides, and recombinant proteins		
DAPI	ThermoFisher	Cat# D1306; RRID:AB_2629482
Lysyl Endopeptidase, LysC	Wako Chemicals	Cat# 129-02541
Trypsin	Thermo Fisher Scientific	Cat# 25200056
Critical commercial assays		
XBridge C18 column	Waters	186003026
Deposited data		
scRNA-seq dataset of developing mouse embryos E9.5-E13.5	https://doi.org/10.1038/s41586-019-0969-x	GSE119945
Spatial transcriptomic dataset of the developing mouse embryos at E8.5, E9.0 and E9.5	https://doi.org/10.1038/s41588-023-01435-6	GSE197353
scRNA-seq dataset of sorted myeloid progenitors in the mouse yolk sac at E9.5	https://doi.org/10.1038/s41586-022-04596-2	GSE195437
Bulk RNA-seq dataset of mouse CNS tissue at E9.5, E14.5 and P60	This paper	GSE249007
LC-MS/MS proteomics dataset of mouse CNS tissue at E9.5, E14.5 and P60	This paper	MSV000097998
Experimental models: Organisms/strains		
Mouse: B6;129-Itgb1tm1Efu/J	The Jackson Laboratory	Cat# JAX:004605; RRID:IMSR_JAX:004605
Mouse: B6.Cg-Commd10Tg(Vav1-icre) A2Kio/J	The Jackson Laboratory	Cat# JAX:008610; RRID:IMSR_JAX:008610
Mouse: B6.129X1-Gt(ROSA)26Sortm1 (EYFP)Cos/J	The Jackson Laboratory	Cat# JAX:006148; RRID:IMSR_JAX:006148
Mouse: B6J.B6N(Cg)-Cx3cr1tm1.1(cre) Jung/J	The Jackson Laboratory	Cat# JAX:025524;RRID:IMSR_JAX:025524
Mouse: *Tln1*$^{fl/fl}$	Kindly provided by T. Lämmermann	N/A
Mouse: B6.129S7-Itgb2tm2Bay/J	The Jackson Laboratory	Cat# JAX:003329; RRID:IMSR_JAX:003329
Mouse: C57BL/6J	The Jackson Laboratory	Cat# #000664; RRID: IMSR_JAX:000664
Oligonucleotides		
Primer: CGG CTC AAA GCA GAG TGT CAG TC Itgb1 fl/fl fw	This paper	N/A
Primer: CCA CAA CTT TCC CAG TTA GCT CTC Itgb1 fl/fl rv	This paper	N/A
Primer: CTA GGC CAC AGA ATT GAA AGA TCT VaviCre int pos ctrl fw	This paper	N/A
Primer: GTA GGT GGA AAT TCT AGC ATC ATC C VaviCre int pos ctrl rv	This paper	N/A
Primer: AGA TGC CAG GAC ATC AGG AAC CTG VaviCre transgene fw	This paper	N/A
Primer: ATC AGC CAC ACC AGA CAC AGA GAT C VaviCre transgene rv	This paper	N/A
Primer: AGGACAGCAAGGGGGAGGATT Itgb2-/- mutant fw	This paper	N/A
Primer: GCC CAC ACT CAC TGC TGC TTG Itgb2-/- WT fw	This paper	N/A

(*Continued on next page*)

Continued

REAGENT or RESOURCE	SOURCE	IDENTIFIER
Primer: CCC GGC AAC TGC TGA CTT TGT Itgb2-/- common rev	This paper	N/A
Primer: AAG CAG GAA CAA AAG TAG GTC TCC Talinfl/fl fw	This paper	N/A
Primer: GCA TCG TCT TCA CCA CAT TCC Talinfl/fl rev	This paper	N/A
Primer: AGC TCA CGA CTG CCT TCT TC Cx3Cr1cre WT fw	This paper	N/A
Primer: GAC ATT TGC CTT GCT GGA C Cx3Cr1cre mutant fw	This paper	N/A
Primer: GCA GGG AAA TCT GAT GCA AG Cx3Cr1cre common rev	This paper	N/A
Primer: CTG GCT TCT GAG GAC CG Rosy1 WT fwd	This paper	N/A
Primer: CAG GAC AAC GCC CAC ACA Rosy2 WT rev	This paper	N/A
Primer: AGG GCG AGG AGC TGT TCA Rosy3 Mut fwd	This paper	N/A
Primer: TGA AGT CGA TGC CCT TCA G Rosy4 Mut rev	This paper	N/A
Software and algorithms		
ImageJ	https://imagej.nih.gov/ij/	RRID:SCR_003070
MaxQuant (v 1.6.14.0)	https://www.maxquant.org/maxquant/	RRID:SCR_014485
NextSeq 2000 Control Software (NCS) v1.4.0.39521	Illumina	RRID:SCR_023614
Real Time Analysis Software (RTA) v3.9.2	Illumina	RRID:SCR_014332
bcl2fastq v2.20	Illumina	RRID:SCR_015058
Trimmomatic (v0.38)	https://www.ncbi.nlm.nih.gov/pmc/articles/PMC4103590/	RRID:SCR_011848
STAR (v2.5.2b)	https://pubmed.ncbi.nlm.nih.gov/23104886/	RRID:SCR_004463
R (v 4.4.0)	https://cran.r-project.org/bin/windows/base/old/4.4.0/	RRID:SCR_001905
limma (v3.65.1)	https://pubmed.ncbi.nlm.nih.gov/25605792/	RRID:SCR_010943
Python (v3.12)	https://www.python.org/downloads/release/python-3120/	RRID:SCR_008394
scanpy	https://pubmed.ncbi.nlm.nih.gov/29409532/	RRID:SCR_018139
pertpy	https://github.com/scverse/pertpy	N/A
milo	https://pubmed.ncbi.nlm.nih.gov/34594043/	RRID:SCR_025630
LIANA+	https://pubmed.ncbi.nlm.nih.gov/39223377/	N/A
CellPhoneDB	https://pubmed.ncbi.nlm.nih.gov/30429548/	RRID:SCR_017054
clusterProfiler	https://pubmed.ncbi.nlm.nih.gov/22455463/	RRID:SCR_016884
Seurat	https://pubmed.ncbi.nlm.nih.gov/29608179/	RRID:SCR_016341
Tidyverse	https://joss.theoj.org/papers/10.21105/joss.01686	RRID:SCR_019186
MSigDB	https://www.pnas.org/doi/10.1073/pnas.0506580102	RRID:SCR_016863

(*Continued on next page*)

CellPress
OPEN ACCESS

Continued

REAGENT or RESOURCE	SOURCE	IDENTIFIER
GraphPad Prism 9	GraphPad Software, Dotmatics	RRID:SCR_002798
FlowJo_v10.7.2	Becton Dickinson Life Sciences	RRID:SCR_008520
ZEN 3.3 (blue edition)	Zeiss	RRID:SCR_013672
Leica Application Suite X	Leica	RRID:SCR_013673

EXPERIMENTAL MODEL AND STUDY PARTICIPANT DETAILS

Animals

C57BL/6J mice from Charles River were used as wildtype mice. All mice including the corresponding wildtype controls were housed in specific pathogen-free conditions and backcrossed on *C57BL/6J* genetic background. Animals were kept in a 12h/12h dark-light cycle and water and food was provided *ad libitum*. All animal experiments were approved by local administration (Regierungspräsidium Freiburg) and were performed in accordance to the respective national, federal and institutional regulations. Transgenic mouse lines including *Itgb2*$^{-/-}$ (*B6.129S7-Itgb2*^{tm2Bay}/J),[55] *Cx3cr1*^{Cre} (*B6J.B6N(Cg)-Cx3cr1*$^{tm1.1(cre)Jung}$/J),[56,57] *Vav*^{iCre} (*B6.Cg-Commd10*$^{Tg(Vav1-icre)A2Kio}$/J),[58] *Tln1*$^{fl/fl}$ (*Tln1*^{tm4Crit}),[59] *Itgb1*$^{fl/fl}$ (*Itgb1*^{tm1Ref}),[60] and *Rosa26*$^{LSL-eYFP}$ (*B6.129X1-Gt(Rosa)26Sor*$^{tm1(EYFP)Cos}$/J)[61] were used in this study. For embryonic stages, both sexes were analyzed. Adult mice in this study were all females.

METHOD DETAILS

Timed matings

Timed matings were used to analyze embryos at defined developmental stages. The matings were started in the evening and separated after vaginal plug check on the following morning. Embryonic development was estimated considering the day of vaginal plug formation as embryonic day (E) 0.5 and staged by developmental criteria.[62] Embryos were dissected at E9.5, E10.5, E12.5, E14.5 or E17.5 as described below. Mating of the different mouse lines is shown in Table S4.

Dissection of embryos

Pregnant female mice were deeply anaesthetized with CO_2 and afterwards sacrificed by cervical dislocation. The whole uterus was removed and each embryo was carefully dissected in ice-cold 1xPBS. For immunohistochemistry, whole embryos were isolated from the uteri at E10.5, E12.5 and E14.5. Tissues were fixed for 6h in 4% paraformaldehyde (PFA). E10.5 embryos were pre-embedded in a 2% agarose and 2.5% gelatine mix prior to dehydration to preserve the tissue structure.[63] For LC/MS-based proteomics and bulk RNA-seq the embryonic heads were cut behind the 4th ventricle and above the forelegs and excessive non-neuroectodermal tissue was removed at E9.5. At E14.5, brains were dissected and the meninges were removed. Directly after dissection, tissues were snap-frozen in liquid nitrogen. For flow cytometry, yolk sacs and heads were sampled at E10.5 (the heads were cut behind the 4th ventricle and above the forelegs). For E12.5, E14.5 and E17.5, brains were dissected and the meninges were removed.

Cardiac perfusion and dissection of adult brains

Adult brains were harvested after transcardial perfusion with 1xPBS. Mice were deeply anaesthetized with a 200 µl intraperitoneal injection of Ketamine (10 %, Essex Tierarznei) and Xylazin ((Rompun) 2 %, Bayer) (100 mg/kg Ketamine and 10 mg/kg Xylazin). Mice were transcardially perfused with 10 ml ice-cold PBS via the left ventricle until the liver was decolourized. Afterwards, the CNS was dissected from the skull and processed for further analysis.

Cell isolation protocol for flow cytometry

Samples from prenatal time points underwent enzymatic digestion to isolate cells for flow cytometry. Samples were transferred to an enzyme mix (PBS with 3% FCS, DNAse (2mg/ml), Collagenase (1mg/ml)), cut into small pieces and digested for 30 min at 37°C. Tissues were further dissociated by passing them through a 100 µm cell strainer into cold FACS buffer (PBS with 5% FCS and 2mM EDTA). The single cell suspension was centrifuged at 320 g for 7 min, 4°C and the resulting cell pellet transferred into a 96-well round bottom plate for staining. Adult brains were mechanically dissociated with a glass potter filled with 10 ml of cold dissection medium (Hank's Balanced Salt Solution (HBSS, Thermo Fisher Scientific), 1,5 % HEPES (1 M) (Thermo Fisher Scientific), 1,3 % Glucose (45 %, Sigma-Aldrich)). Samples were then strained with a 70 µm cell strainer and transferred into 10 ml of 37 % Percoll (100 %, Sigma-Aldrich). The density gradient was centrifuged for 30 minutes at 400 g at 4 °C without brake. Afterwards the cell pellet was transferred into a 96-well round bottom plate for staining.

Cell staining for flow cytometry and analysis

Cells were incubated for 20 min on ice with Fc receptor blocking antibody anti-CD16/32 (clone 2.4G2, BD Biosciences, 1:200) to prevent non-specific antibody binding. Afterwards, the cell suspension was stained for 20 min with different antibody mixes at a dilution

of 1:200. To gate on embryonic microglia at E14.5 and E17.5 and adult microglia, cells were stained with anti-CD45 (clone 30-F11, eBioscience) antibody, anti-F4/80 (clone BM8, BioLegend) and an anti-CD11b (clone M1/70, BioLegend) antibody. For yolk sac progenitors and embryonic microglia at E10.5 anti-ckit (clone 2B8, BDBiosciences) was additionally used. To measure integrin expression, we used an anti-α_2 (clone HMα2, BD Biosciences) antibody, anti-α_{IIb} (clone eBioMWReg30, eBioscience) antibody, anti-α_4 (clone R1-2, eBioscience) antibody, anti-α_5 (clone 5H10-27, life technologies) antibody, anti-α_6 (clone eBioGoH3, eBioscience) antibody, anti-α_L (clone M17/4, eBioscience) antibody, anti-α_V (clone RMV-7, eBioscience) antibody, anti-α_X (clone N418, eBioscience) antibody, anti-α_E (clone 2E7, eBioscience) antibody, anti-β_1 (clone eBioHMb1-1, eBioscience) antibody, anti-β_2 (clone C71/16, BD Biosciences) antibody, anti-β_3 (clone 2C9.G3, eBioscience) antibody, anti-β_4 (clone 346-11A, BioLegend) antibody, anti-β_5 (clone KN52, eBioscience) antibody, as well as an anti-β_7 (clone FIB504, eBioscience) antibody. As isotype controls we used rat IgG1 κ isotype control (clone RTK2071, BioLegend), rat IgG2b κ isotype control (clone A95-1, BD Biosciences) antibody, rat IgG2a κ isotype control (clone R35-95, BD Biosciences) antibody, armenian hamster isotype control (clone eBio299Arm, eBioscience) antibody and-mouse IgG1 isotype control (clone A85-1, BD Biosciences) antibody. From E12.5 onwards, we included a dump channel with anti-Gr1 (clone RB6-8C5, BD Biosciences), anti-CD3e (clone 17A2, BioLegend) and anti-CD19 (clone 6D5, BioLegend). Dead cells were excluded via fixable viability dye 780 (Invitrogen) (1:1000) or 4',6-diamidino-2-phenylindole (DAPI) (Sigma-Aldrich)(1:5000). After two washing steps, cells were resuspended in 200 µl FACS buffer and acquired on a SORP BD LSRFortessa™ using the BD FACSDiva Software v9.0.1. For compensation between channels, compensation beads (Thermo Fisher) were stained in 400 µL FACS buffer using the same direct coupled antibodies individually at a dilution of 1:400. Analysis was performed with FlowJo_v10.9.0.

Chromogenic Immunohistochemistry

Embryos and adult brains were fixed for 6h in 4% PFA, washed with PBS and dehydrated by immersion in an ethanol-series. The samples were then embedded in paraffin. Using a microtome, samples were cut in 7 µm thick sections. Paraffin was removed by incubating slides at 80 °C for 40 min and further deparaffinized by dipping into a series of xylene and graded alcohol to H_2O. Antigen retrieval was performed at pH 6 for 40 min. Samples were treated for 10 min with 3% hydrogen peroxide in TRIS buffer, blocked with PBS containing 10% bovine serum albumin and permeabilized with 0.1% Triton-X. Primary antibody Iba1 (ab178846, abcam, EPR16588) was added overnight at a dilution of 1:1000 at 4 °C. The biotinylated anti-rabbit IgG secondary antibody (Sigma-Aldrich, B9642) was added at a dilution of 1:300 for 45 min at RT. Streptavidin-horseradish-peroxidase (dilution 1:1000 in TRIS buffer) was added for 45 min at RT. Afterwards, 3,3′-Diaminobenzidine was diluted (1 drop in 1 ml Envision Flex substrate buffer) and added until the reaction, leading to a brown color, was sufficient. Counterstaining of nuclei was performed by dipping the samples into a Gill's hematoxylin solution for a few seconds (about 5 sec). The stainings were then washed under running water and placed in an ascending alcohol series. As a final step, the slides were mounted with the quick-hardening mounting medium Vitro-Clud® (Langenbrinck). Images were acquired with a Zeiss Axioscan.

Immunofluorescence stainings and imaging

Embryos were fixed for 6h in 4% PFA and dehydrated by incubation in 30% sucrose for 4-5 days. Samples were embedded in Tissue-Tek® O.C.T. Compound and frozen with dry ice in ethanol. At E10.5, embryos were pre-embedded in a mix of 2% low melting agarose and 2,5% gelatin to further protect the tissue. Samples were cut with a cryostat (Leica) in 20 µm thick sections. Sections were stained in a vertical staining chamber. Therefore, sections were blocked for 2h with 1 ml of blocking buffer (0.5% BSA, 5% normal goat serum, 0.3% Triton X-100 in 1x PBS). Sections were then incubated overnight at 4°C in an antibody mix (Iba-1 1:500 (clone Gp311H9, guinea pig, Synaptic Systems); Laminin 1:500 (polyclonal, rabbit, Merck); CD206 1:500 (clone MR5D3, rat, BioRad) in 150 µl PBS, 0.1% Triton X-100, 0.5% BSA). Sections were washed three times with PBS and secondary antibody mix was added (goat anti-guinea pig Alexa Fluor® 488 1:1000, Invitrogen; goat anti-rabbit Alexa Fluor® 568 1:1000, Invitrogen; goat anti-rat Alexa Fluor® 647 1:1000, Invitrogen; DAPI 1:5000) in 150 µl PBS, 0.1% Triton X-100, 0.5% BSA) for 2h at RT. Samples were washed again three times with PBS and mounted with Mowiol®. The sections were imaged on a Leica THUNDER fluorescence microscope. Images were acquired using a 20× 0.8 NA (HC PL APO 20×/0.80 DRY) lens, with a Z-step size of 4 µm (overview) and 1 µm (close-up), respectively.

Liquid chromatography – tandem mass spectrometry (LC-MS/MS) analysis

Tissue specimen of murine CNS were prepared as described previously[64] with the following modifications: Proteins were double digested with LysC (Wako) for 2 h at 42°C and Trypsin (Serva) overnight at 37°C. After peptide clean-up and TMT-labeling, peptides were separated using high pH reverse phase liquid chromatography (RPLC). To this end, all TMT-labeled samples were pooled and loaded on an XBridge C18 column (150 mm × 1 mm column containing 3.5 µm particles, Waters). An increasing linear gradient of acetonitrile from 10% to 50% over 42 min at a flowrate of 250 µL/min was applied using an Äkta Explorer 900 System. 40 fractions were collected and concatenated into 10 fractions (combining fraction 1 with 11, 21 and 31, fraction 2 with 12, 22 and 32, and so on). The resulting 10 samples were vacuum-concentrated until dryness and stored at -80°C until liquid chromatography – tandem mass spectrometry (LC-MS/MS) analysis. LC-MS/MS analysis was performed as described previously.[64] Raw data were analyzed using MaxQuant (v 1.6.14.0). For peptide identification, the Andromeda search engine was used with the mouse reference proteome (downloaded from EMBL-EBI on 9th May, 2020) (22,306 entries). Further data analysis settings were as described previously.[64] Statistical analysis of the MaxQuant output was performed in R (v 4.0.0) using linear models for microarray data (LIMMA) with an adjusted pvalue cut-off set at 0.05. The TopGO package was used to probe gene ontology protein set over-representation.[65] The enrichment

of extracellular matrix-related gene sets were evaluated using an in-house R script which implements a Roast function from the LIMMA package and the NABA database (C2 subset of MSigDb with focus on extracellular matrix proteins).[31]

Bulk RNA-sequencing

RNA extraction, library preparation and RNAseq were performed at the Genomics Core Facility "KFB - Center of Excellence for Fluorescent Bioanalytics" (University of Regensburg, Regensburg, Germany; www.kfb-regensburg.de). Total RNA was extracted from dissected brain tissue at E9.5, E14.5 and P60 stabilized in RLT buffer according to the "Purification of total RNA from animal and human cells" protocol of the RNeasy Micro Kit (QIAGEN, Hilden, Germany). In brief, cells were stored in buffer RLT containing 1% beta-mercaptoethanol and shipped on dry ice. After thawing, the samples were homogenized by vortexing for 1 min. Next, one volume of 70 % ethanol was added and the samples were applied to RNeasy MinElute spin columns, followed by an on-column DNase digestion and several wash steps. Finally, total RNA was eluted in 14 µl of nuclease free water. Purity and integrity of the RNA was assessed on the Agilent 2100 Bioanalyzer with the RNA 6000 Pico LabChip reagent set (Agilent, Palo Alto, CA, USA). The SMARTer Ultra Low Input RNA Kit for Sequencing v4 (Clontech Laboratories, Inc., Mountain View, CA, USA) was used to generate first strand cDNA from approximately 1 ng total-RNA. Double stranded cDNA was amplified by LD PCR (11 cycles) and purified via magnetic bead clean-up. Library preparation was carried out as described in the Illumina Nextera XT Sample Preparation Guide (Illumina, Inc., San Diego, CA, USA). Thereby 150 pg of input cDNA were tagmented (tagged and fragmented) by the Nextera XT transposome. The products were purified and amplified via a limited-cycle PCR program to generate multiplexed sequencing libraries. For the PCR step, 1:5 dilutions of the unique dual indexing (i7 and I5) adapters were used. The libraries were quantified using the KAPA Library Quantification Kit - Illumina/ABI Prism User Guide (Roche Sequencing Solutions, Inc., Pleasanton, CA, USA). Equimolar amounts of each library were sequenced on an Illumina NextSeq 2000 instrument controlled by the NextSeq 2000 Control Software (NCS) v1.4.0.39521, using one 50 cycles P3 Flow Cell with the dual index, single-read (SR) run parameters. Image analysis and base calling were done by the Real Time Analysis Software (RTA) v3.9.2. The resulting.cbcl files were converted into.fastq files with the bcl2fastq v2.20 software.

Bulk RNA-sequencing analysis

Single end reads were first trimmed with Trimmomatic (v0.38) to remove bad quality reads and adapter content.[66] The following parameter were used: HEADCROP:3 TRAILING:10 MINLEN:25. Reads were then aligned to the mouse reference genome (mm10) and quantified using STAR (v2.5.2b).[67] STAR parameter were set as follow: –outFilterMultimapNmax 10 –alignSJoverhangMin 8 –alignSJDBoverhangMin 1 –outFilterMismatchNmax 999 –outFilterMismatchNoverLmax 0.05 i–alignIntronMin 20 –alignIntronMax 1000000 –alignMatesGapMax 1000000 –outFilterMatchNmin 16 –quantMode GeneCounts. Bulk RNA-sequencing raw counts were normalized using library size and trimmed mean of M values (TMM) normalization factor. Genes that were quantified in less than 2 samples were discarded. Differential expression analysis was performed using a linear model-based approach with the limma R package.[68] Fisher exact test was used to assess the over-representation of gene-sets within the top regulated genes (adjusted p value <0.05 and absolute log2 fold change >5). The reference gene-sets from MSigDB were used, including gene ontology (GO).[69] In both analyses, adjusted p value below 0.05 was considered as significant.

Single cell RNA-sequencing of yolk sac progenitors and analysis

Yolk sac progenitors from eight individual yolk sac (E9.5) were isolated and sorted in a 384-well plate containing lysis buffer and barcodes. Single cell RNA-sequencing and subsequent analysis were described in detail here: Masuda et al.[20] The presented dataset includes gene expression profiles of 483 macrophage progenitors. Gene ontology (GO) analysis was preformed using the clusterProfiler R package version 4.12.6.[70] Cluster marker genes were identified using the FindAllMarkers() function in the Seurat R package. Top 100 genes were selected based on the average log2-fold change value using the group_by() and top_n() functions within the tidyverse R package version 2.0.0. Genes were converted to ENTREZIDs using the bitr() clusterProfiler function. Cluster-wise GO terms for biological functions were identified using the compareCluster function of the clusterProfiler package. The fun parameter of the function was set to "EnrichGO". This parameter calculates the enrichment of GO terms after false discovery rate (FDR) control. Adjusted p values below 0.05 were considered statistically significant. We visualized cluster-wise terms using the dotplot function of the clusterProfiler package. GO term gene signatures were calculated using the AddModuleScore function of the Seurat R package. Briefly, the function determines the average expression levels of each signature (or cluster) at the single-cell level and then subtracts the aggregated expression of control feature sets. To ensure comparability, all analyzed features are grouped into bins based on their average expression levels, and control features are randomly chosen from within each bin. For gene ontology over-representation testing, we used a hypergeometric test implemented in the clusterProfiler package.[71] p values for over-representation were adjusted for multiple testing with the Benjamini Hochberg method with an adjusted p value cutoff of 0.05. scRNA-seq datasets have been uploaded to the gene expression omnibus database (GEO) under the accession number GSE195437. The code for the scRNA-seq analysis of yolk sac macrophage progenitors is available at https://github.com/rsankowski/Taka_A1_A2_only.

Analysis of spatial transcriptomic and scRNA-seq data set of whole mouse embryos

Analyses of a recently published spatial transcriptomic[33] and a published single-cell RNA-sequencing dataset[28] of the developing mouse embryo were conducted. All analyses were performed in Python using tools from the scverse ecosystem.[72] We loaded the publicly available AnnData objects and utilized the original authors' cell annotations as initial references. These annotations were

further refined by comparing them with our defined microglia progenitor signature (e.g. *Aif1*, *Irf8*, *Csf1r*, *Itgam*, *Mrc1*, *Cx3cr1*) using Scanpy.[73]

For the scRNA-seq data analysis, we performed additional sub-clustering of the microglia progenitor signature enriched cell cluster C31 using the Leiden clustering algorithm.[74] A cluster-free differential abundance analysis was conducted using Milo through the Pertpy interface to compare different developmental stages.[29,75] Additionally, cell-cell communication prediction analysis was inferred by matching ligand and receptor expressions using CellPhoneDB accessed via the LIANA interface.[30,76]

The code for both analyses is available at https://github.com/MerktSimon/analysis_publ_data_petry_et_al.

QUANTIFICATION AND STATISTICAL ANALYSIS

Statistical significance of microglia quantification, comparison of Itgb1 and Itgb2 expression on yolk sac progenitors as well as eYFP labeling efficiency were tested for significant differences between groups with an unpaired t-test or one-way ANOVA as indicated in the figure legends. Asterisks indicate the following significance levels: *p<0.05, **p<0.01, ***p<0.001, ****p<0.0001. Non-significant comparisons are labeled with ns. Statistical tests were performed using GraphPad Prism 9 software.